Acta Pharmaceutica Sinica B 2026;16(8):5328−5350

Chinese Pharmaceutical Association
Institute of Materia Medica, Chinese Academy of Medical Sciences

Acta Pharmaceutica Sinica B

www.elsevier.com/locate/apsb
www.sciencedirect.com

ORIGINAL ARTICLE

Targeting NAT10 with Remodelin reshapes the pro-fibrotic microenvironment in renal fibrogenesis *via* inhibiting exosome oversecretion from tubular cells

Yuqin Tan[a,†], Jiaojiao Zheng[b,†], Ruojiao Wang[a,†], Zhaozhong Zhong[a,†], Suxiang Chen[c], Shuo Lu[a], Jiayu Zheng[a], Yongrong Ye[a], Ning Na[a,*], Tong Zheng[a,*]

[a]*Department of Kidney Transplantation, The Third Affiliated Hospital of Sun Yat-sen University, Guangzhou 510630, China*
[b]*State Key laboratory of Oncogenes and Related Genes, Shanghai Cancer Institute, Renji Hospital, Shanghai Jiao Tong University, School of Medicine, Shanghai 200127, China*
[c]*Centre for Molecular Medicine and Innovative Therapeutics, Murdoch University, Perth, Western Australia 6150, Australia*

Received 9 February 2025; received in revised form 7 August 2025; accepted 27 August 2025

KEY WORDS

Renal fibrosis;
Fibroblast activation;
Exosomes;
Acetylation;
NAT10;
ac4C;
Remodelin;
Cell-cell communication

Abstract Renal fibrosis induces irreversible renal failure and lacks therapies. The tubular epithelial cells (TEC) largely depend on exosomes to create a pro-fibrotic microenvironment, initiating fibroblast activation. However, how exosome secretion of TEC is over-activated during renal fibrogenesis remains unknown. Herein, *in vitro* high-throughout screen uncovered acetyltransferase NAT10 as promising target to interfere with TEC-fibroblast communication. Further experiments showed that NAT10 was upregulated mainly in the TEC of fibrotic kidneys, and its conditional depletion in TEC alleviated renal fibrosis *in vivo*. Mechanistically, nuclear NAT10 coordinated with cytoplasmic NAT10 to promote exosome secretion of TEC to induce fibroblast activation *via* combining mRNA ac4C modification and lysine acetylation (Kac). Moreover, NAT10 upregulated the abundance of exosomal Gli in TEC, which were vital for

*Corresponding authors.
E-mail addresses: naning@mail.sysu.edu.cn (Ning Na), zhengt57@mail.sysu.edu.cn (Tong Zheng).
[†]These authors made equal contributions to this work.
Peer review under the responsibility of Chinese Pharmaceutical Association and Institute of Materia Medica, Chinese Academy of Medical Sciences.

https://doi.org/10.1016/j.apsb.2026.05.020

fibroblast activation. In summary, NAT10-mediated orchestration of ac4C and Kac modifications is the mechanism of over-activated exosome secretion of TEC during renal fibrogenesis. And targeting NAT10 with Remodelin is a promising therapy for renal.

1. Introduction

Renal fibrosis, characterized by fibroblast overactivation and thus extracellular matrix (ECM) overproduction, is the common ending of chronic kidney diseases (CKD)[1]. Although renal fibrosis leads to irreversible renal failure, its effective therapy remains almost blank.

Fibroblast activation is the decisive step of renal fibrosis. Tubular epithelial cell (TEC), is both the most abundant cell type in kidney and the most vulnerable one upon injury. The injured TEC is the origin of fibroblast activation *via* paracrine effect, forming a pro-fibrotic TEC−fibroblast chain. Exosome, one of the smallest extracellular vesicles (EVs), mediates the TEC−fibroblast chain *via* activating Sonic hedgehog (SHH)−Gli signaling[2]. Especially, the exosome secretion of TEC is over-stimulated during renal fibrogenesis[3,4]. Therefore, exosome targeting is a promising strategy to break the TEC−fibroblast chain. Although TGF-β was reported as stimulus of exosome secretion[5,6], how exosome secretion of TEC is overactivated remains unknown.

RNA modification, the main component of epitranscriptomics, is an emerging participator in renal fibrosis[7]. Previous studies found that dysregulation of alternative polyadenylation (APA)[8-10] and N^6-methyladenosine (m6A)[11,12], the most abundant types of mRNA modification, promotes various renal disorders including renal fibrosis. These findings emphasize the therapeutic potential of utilizing epitranscriptomics for renal fibrosis. In addition, N^4-acetylcytidine (ac4C), catalyzed by *N*-acetyltransferase 10 (NAT10) alone, is another widespread RNA modification. NAT10−ac4C axis promotes mRNA stability and/or translational efficiency[13,14], and its dysregulation is implicated in many pathologies[15-17]. Unlike the other writers of RNA modifications, NAT10 is also capable of catalyzing lysine acetylation (Kac). However, to date, the published studies involving NAT10 all partially focused on ac4C or Kac. How NAT10 orchestrate ac4C and Kac remains unknown. As a protein primarily localized in nucleus, whether NAT10 in other subcellular compartments acquires distinct physiological or pathological functions remains poorly explored.

Here, we investigated how to break the pro-fibrotic TEC-fibroblast chain *via* high-throughout screen and clinical analysis, identifying NAT10 as a promising target. NAT10 was found upregulated mainly in TEC by TGF-β during renal fibrogenesis, and specific deletion of NAT10 in TEC suppressed fibroblast activation and renal fibrosis. Mechanistically, nuclear NAT10−ac4C axis coordinated with cytoplasmic NAT10−Kac axis to stimulate exosome secretion of TEC, thus favoring the TEC−fibroblast chain. Besides, we uncovered that NAT10 also elevated the abundance of exosomal Gli2, which was indispensable for fibroblast activation. Finally, NAT10 inhibitor Remodelin was a promising therapy for renal fibrosis.

2. Materials and methods

2.1. Cell culture and treatments

Human kidney tubular epithelial cell HK-2 were cultured in DMEM/F-12 medium (Gibco, NY, USA) containing 10% FBS (Gibco, NY, USA). Human embryonic kidney cell 293T, NRK-49F cells, 786-O cells and A498 cells were cultured in DMEM medium (Gibco, NY, USA) containing 10% FBS (Gibco, NY, USA). Caki-1 cells were cultured in McCOY's 5A medium (VivaCell, Shanghai, China) containing 10% FBS (Gibco, NY, USA). EL4 cells were cultured in IMDM with GlutaMax (Gibco, NY, USA) containing 5% FBS, and primary T cells were cultured in RPMI 1640 medium with L-glutamine (Gibco, NY, USA) containing 10% FBS. All cells were incubated at 37 °C in a humidified atmosphere with 5% CO_2. $CD4^+CD25^-$ T cells and $CD4^+CD25^+$ Treg cells were purified as previously reported[18]. For cell treatment, TGF-β (Peprotech, NJ, USA) and Remodelin (MCE, NJ, USA) were used with indicated doses.

2.2. Isolation of mouse kidney proximal tubule epithelial cells (PTECs)

Mouse kidney proximal tubule epithelial cells (PTECs) were isolated as previously described[19,20]. Briefly, mouse kidneys were removed immediately and placed in cold DMEM/F-12 medium to remove blood. The cortical tissue was dissected and minced into small pieces ($\sim$1 mm^3). Minced tissue was washed with cold 1 × PBS buffer, transferred to collagenase solution (1 mg/mL; Sigma, MO, USA) and incubated for 60 min at 37 °C. After incubation, the supernatant was sieved through a 100-μm mesh filter to remove undigested tissue, and then followed by a 40-μm mesh filter. The pellet on the 40-μm mesh filter was collected and centrifuged at 150×*g* for 10 min. The cells were resuspended and seeded onto culture dishes pre-coated with type IV collagen (Corning, NY, USA). Cells were maintained in DMEM/F-12 medium and incubated at 37 °C in a humidified atmosphere with 5% CO_2.

2.3. High-throughout compound screen and cell viability

HK-2 cells were seeded in 96-well plates at the density of 10,000 cells per well, and then treated with TGF-β (5 ng/mL) in the presence of each inhibitor (1 or 5 μmol/L) of Epigenetic Compound Library (TargetMol, MA, USA). After the treatment,

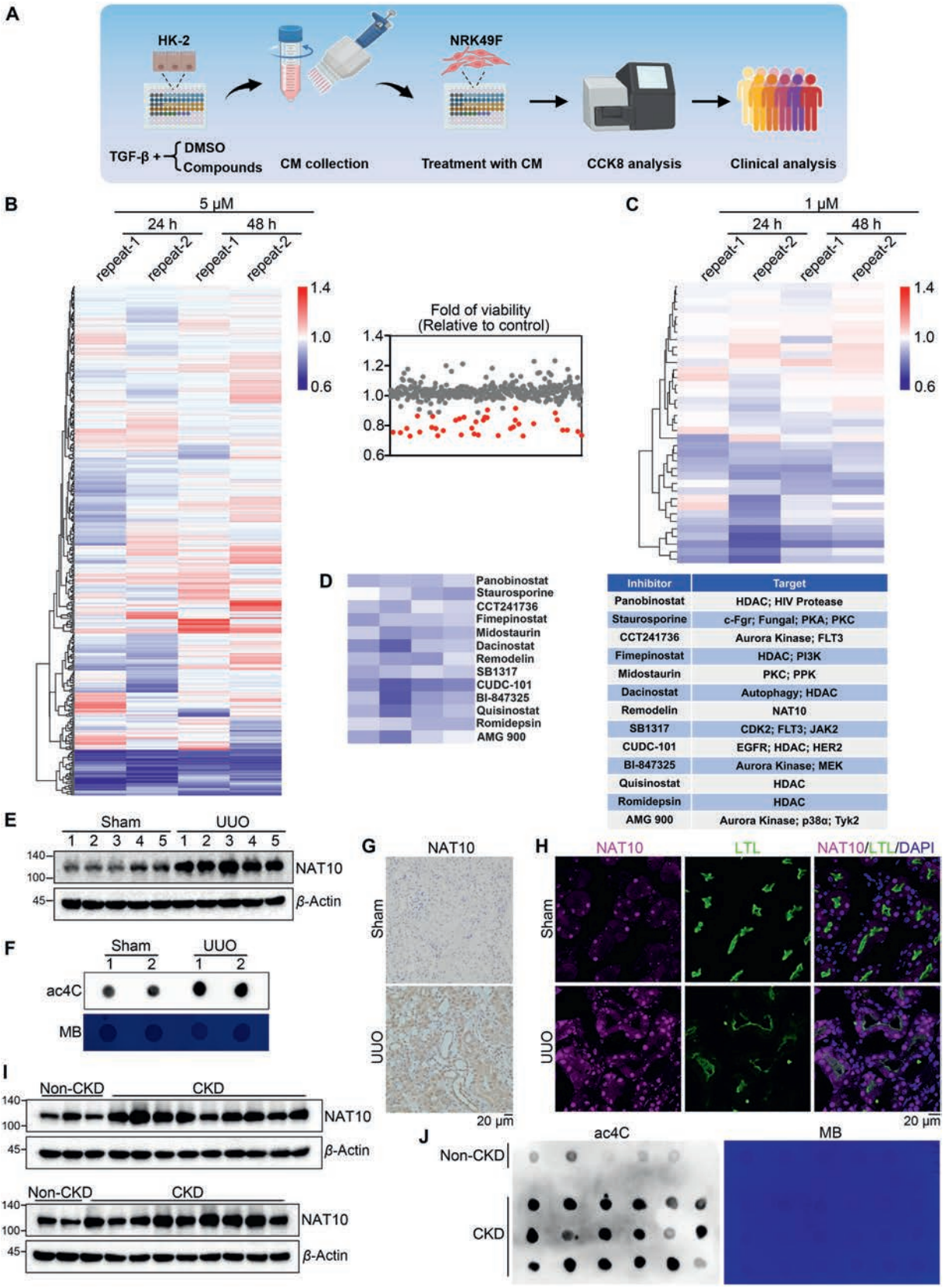

Figure 1 Targeting acetyltransferase NAT10 with Remodelin breaks the TEC-fibroblast pro-fibrotic chain (A) The graph indicating the selection strategy of screen based on *in vitro* model of TEC-fibroblast communication with epigenetic inhibitor compounds. (B) The heatmap of viability of NRK-49F cells incubated with CM from HK-2 cells with indicated treatments respectively (left panel). The dots indicated the average fold of viability of NRK-49F cells incubated with CM from HK-2 cells treated with TGF-β and epigenetic inhibitors, in relative to the NRK-49F

the medium was aspirated and cells were incubated with fresh serum-free medium for additional 48 h. Then the conditioned media (CM) was collected to treat NRK-49F.

Cell viability of the indicated NRK-49F cells was determined using CCK8 method. Briefly, NRK-49F cells were seeded in 96-well plates at the density of 5000 cells in 100 μL per well and then treated with CM collected from HK-2 cells. After treatment, cell viability was measured using the CCK8 assay kit (MCE, NJ, USA) according to the manufacturer's instructions.

2.4. Quantitative real-time PCR

Total RNA was extracted from cells with TRIzol reagent (Sigma, MO, USA) and reversely transcribed into cDNA with SuperScript III Reverse Transcriptase Kit (Invtriogen, CA, USA) following the manufacturer's instructions. The qRT-PCR assays were performed with SYBR-GREEN (Roche, Basel, Switzerland). The primers are listed in Supporting Information Table S1.

2.5. Histology, immunohistochemistry and Sirius Red staining

Histology and immunohistochemistry were performed as previously reported[9]. Briefly, kidney tissues were embedded in paraffin, cut into 5-μm sections and placed on slides. The slides were dewaxed with xylene, rehydrated with gradient ethanol for 5 min and soaked in distilled water twice. For histological analysis, the slides were stained with hematoxylin and eosin (H&E). For immunohistochemical analysis, after antigen retrieval, the slides were cooled naturally to room temperature. 3% hydrogen peroxide was used to incubate the slides for 20 min. Then the slides were incubated with 10% normal goat serum at 37 °C for 60 min. Next, the slides were incubated with specific primary antibodies at 4 °C overnight. After washing with 1 × PBS buffer, the slides were incubated with a universal two-step detection kit including secondary antibody (ZSGB-BIO, Beijing, China) for 1 h. After incubation with DAB (KeyGEN, Nanjing, China), the slides were rinsed with running water for 30 min and stained with hematoxylin.

Sirius Red staining was performed using Picrosirius Red (Servicebio, Wuhan, China). Briefly, kidney tissues were embedded in paraffin, cut into 5-μm sections and placed on slides. The slides were dewaxed with xylene, rehydrated with gradient ethanol and soaked in distilled water twice. Then the slides were incubated with Picrosirius Red for 30 min. After staining, the slides were washed with 1 × PBS buffer, dehydrated with gradient ethanol, cleared with xylene and sealed with neutral resin.

2.6. Immunofluorescence (IF) staining

IF staining was performed as previously reported[9]. Briefly, the cells or kidney cryosections were fixed with 4% paraformaldehyde (PFA) and permeabilized with 0.2% Triton X-100. After blocking with 10% normal goat serum, the cells or kidney cryosections were co-immunostained respectively with primary antibodies overnight at 4 °C. After incubation with secondary antibody for 1 h at 37 °C, the nuclei were stained with DAPI and the staining was evaluated with confocal microscope Leica TSC SP8 (Leica, HE, Germany).

2.7. Immunoblot analysis

Immunoblot was performed as previously reported[9]. Briefly, the cells or kidney tissues were homogenized with RIPA lysis buffer containing Tris−HCl, NaCl, SDS, sodium deoxycholate, NP-40, Protease Inhibitor Cocktail and phosphatase inhibitor. Protein concentration was determined using BCA assay kit (Beyotime, Beijing, China).

Equivalent amounts (20 μg) of protein sample from tissues and cells were separated by polyacrylamide gel electrophoresis using a Mini PROTEAN® Tetra Cell western system (Bio-Rad, CA, USA) and transferred to PVDF membranes. Then the PVDF membranes were incubated with 1 × PBS buffer containing 5% non-fat dry milk and 0.5% Tween for blocking. The membranes were immunoblotted respectively with specific primary antibodies. After incubation with secondary antibodies, the membranes were imaged using ECL Western Blotting Substrate (Vazyme, Nanjing, China) and a chemiluminescence imager (G:Box chemi XX6, Syngene, Cambridge, UK).

2.8. Dot blot

The total RNA was denatured by heating for 5 min at 65 °C and chilled on ice immediately for 1 min. Then the RNA samples were transferred to Hybond-N^+ membrane using a 10-μL tip. The membranes were cross-linked by UV at 254 nm with a dose of 150 mJ/cm^2, blocked by 5% non-fat dry milk for 1 h at room temperature, and incubated with anti-ac4C antibody (Abcam, Cambridge, UK) over night at 4 °C. After incubation with secondary antibody for 1 h at 37 °C, the membranes were imaged.

2.9. Acetylated RNA immunoprecipitation sequencing

Total RNA was extracted from wild-type (WT) and NAT10-depleted ($NAT10^{-/-}$) HK-2 cells. Extracted RNA underwent rRNA depletion using Ribo-Zero Gold rRNA Removal Kit (Illumina, CA, USA). rRNA-depleted RNA was subjected to immunoprecipitation using the GenSeq™ ac4C-IP Kit (GenSeq, Shanghai, China) according to the manufacturer's protocol. Briefly, RNA was randomly fragmented to ∼200 nt using chemical fragmentation reagents. Protein A/G magnetic beads were conjugated with anti-ac4C antibody by rotation at room temperature for 1 h. Fragmented RNA was incubated with the antibody-conjugated beads at 4 °C for 4 h with rotation. RNA/antibody

cells incubated with CM from HK-2 cells treated with TGF-β and DMSO (right panel). The red dots indicated the selected inhibitors for further screen. (C) The heatmap of viability of NRK-49F cells incubated with CM from HK-2 cells with indicated treatments, respectively. (D) The heatmap (left) and table (right) demonstrating the details of 13 effective epigenetic inhibitors. (E) The immunoblot analysis of NAT10 in kidneys from sham mice ($n = 5$) and UUO mice ($n = 5$). (F) The dot blot analysis of ac4C in kidneys from sham mice ($n = 2$) and UUO mice ($n = 2$). (G) The immunohistochemistry staining of NAT10 in kidneys from sham mice and UUO mice. (H) The immunofluorescence staining of NAT10 in kidneys from sham mice and UUO mice. LTL was used as marker of proximal tubular cells. (I) The immunoblot analysis of NAT10 in kidneys from CKD patients ($n = 18$) and non-CKD control ($n = 5$). (J) The dot blot analysis of ac4C in kidneys from CKD patients ($n = 18$) and non-CKD control ($n = 5$). Data are presented as mean ± SD. Student's t test was used for comparison between two groups and one-way ANOVA was used for comparison between multiple groups; $^*P < 0.05$; $^{**}P < 0.01$; $^{***}P < 0.001$.

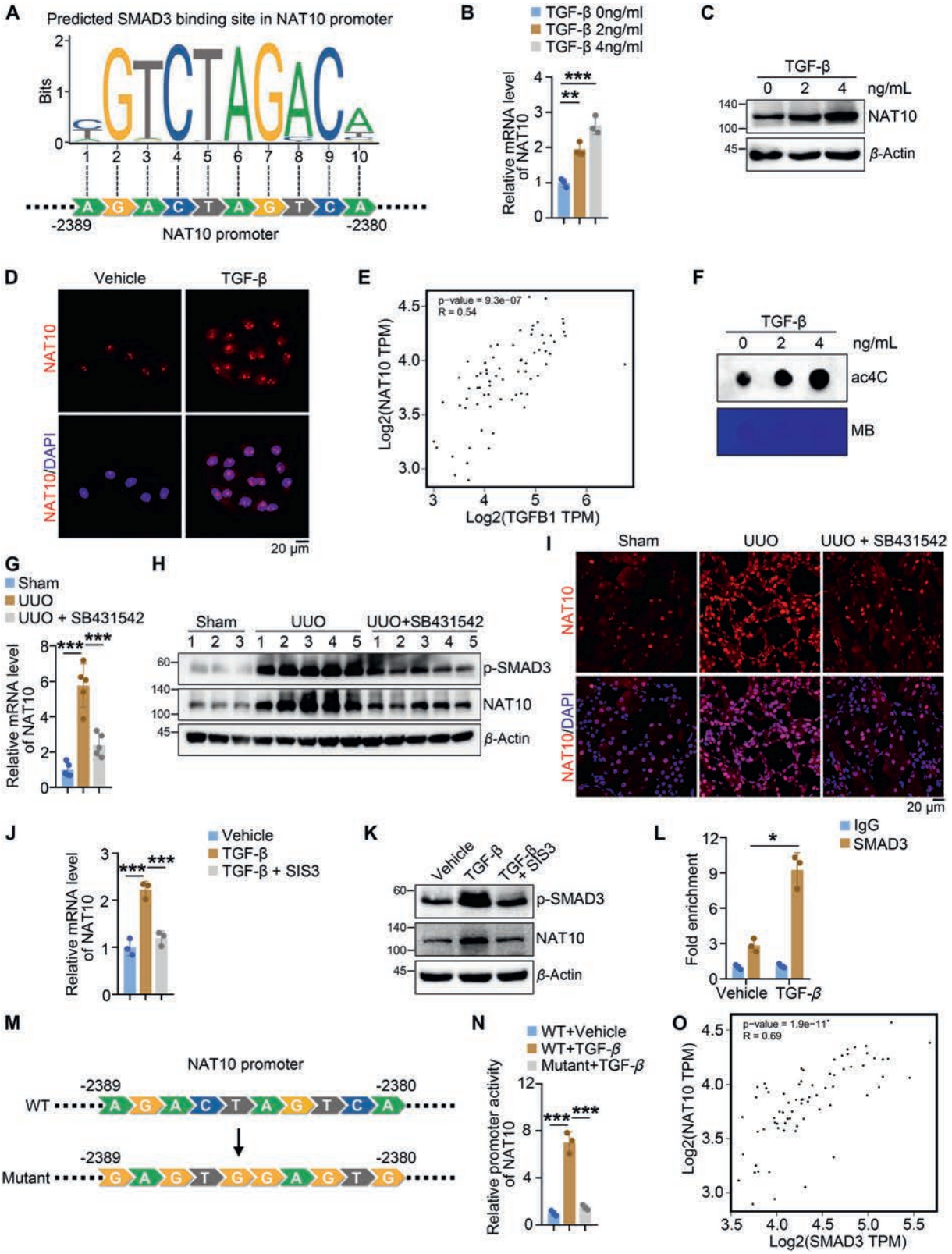

Figure 2 TGF-β−Smad3 signaling is responsible for NAT10 upregulation in TEC during renal fibrogenesis. (A) The graph indicating the canonical Smad3 binding motif in NAT10 promoter. (B) The qRT-PCR analysis of NAT10 was performed in HK-2 cells treated with indicated doses of TGF-β ($n = 3$). (C) The immunoblot analysis of NAT10 was performed in HK-2 cells treated with indicated doses of TGF-β. (D) The immunofluorescence staining was performed in HK-2 cells with or without TGF-β treatment. (E) The analysis of relationship between TGF-β expression and NAT10 expression was performed in human kidneys *via* GEPIA Database. (F) The dot blot analysis of ac4C was performed in HK-2 cells treated with indicated doses of TGF-β. (G) The qRT-PCR analysis of NAT10 was performed in

complexes were digested with Proteinase K. Immunoprecipitated RNA was eluted and purified by phenol: chloroform extraction. RNA libraries for both IP and input samples were then constructed using the NEBNext Ultra II Directional RNA Library Prep Kit (NEB, MA, USA), following the manufacturer's instructions. Library quality was assessed using an Agilent 2100 Bioanalyzer. Qualified libraries were sequenced on an Illumina HiSeq platform, generating paired-end reads (2 × 150 bp) on an Illumina NovaSeq 6000 sequencer. After 3′ adaptor trimming, low-quality reads were removed using cutadapt (v1.9.3). After that, clean reads from all libraries were aligned to the reference genome (*e.g.*, hg38/GRCh38) using HISAT2 (v2.0.4). Acetylated RNA sites (peaks) were identified using MACS2 software. Differentially acetylated sites (DAS) between WT and NAT10$^{-/-}$ groups were identified using diffReps. These peaks identified by both MACS2 and diffReps that overlapped with mRNA exons were selected using custom Python/R scripts. Peaks were called with fold-change >2 ($\log_2$FC > 1) and FDR <0.05, achieving an IDR <0.01 across replicates. KEGG pathway enrichment analyses were performed on protein-coding genes harboring differentially acetylated sites. The ac4C RNA immunoprecipitation sequencing (acRIP-seq) service was provided by Cloud-Seq Inc (Shanghai, China)[21].

2.10. Chromatin immunoprecipitation (ChIP)

ChIP was performed as previously reported[22]. Briefly, after TGF-β treatment, HK-2 cells were crosslinked with 1% formaldehyde for 10 min at 37 °C and quenched with glycine with a final concentration of 125 mmol/L. After rinsing with Cold PBS twice, the cells were sonicated to shear DNA to 200−600 bp fragments. The antibody against Smad3 (CST, MA, USA) was used for immunoprecipitation. qRT-PCR was used to analyze the amounts of Smad3-bound NAT10 promoter. The primers used in ChIP are listed in Supporting Informaiton Table S1.

2.11. Exosome isolation, identification, NTA and TEM

To isolate exosomes from the supernatant of HK-2 cells, cells were cultured in serum medium until the cell density reached 70%−80%. Then serum medium was removed. HK-2 cells were washed three times with 1 × PBS and cultured in exosome-depleted serum-free medium for 48 h. Briefly, the medium was collected and centrifuged at 300×*g* for 10 min at 4 °C to remove cells. The supernatant was moved carefully into a new centrifuge tube and centrifuged again at 3000×*g* for 15 min at 4 °C to ensure that the cells or cell debris were removed (Allegra X-14R, Beckman Coulter, CA, USA). Then the supernatant was moved carefully into a new centrifuge tube and centrifuged at 10,000×*g* for 40 min at 4 °C for the efficient removal of vesicles with large diameters (J2-HS, Beckman Coulter, CA, USA). The resulting supernatant was filtered through a 0.45-μm filter and centrifuged again at 10,000×*g* for 70 min at 4 °C. The supernatant was removed and the pellet was resuspended in 1 × PBS and filtered through a 0.22-μm filter. Then the exosome pellet was collected by centrifugation at 100,000×*g* for 70 min at 4 °C. Finally, the exosome pellet was resuspended in 1 × PBS or lysis buffer for further analysis. For the analysis of purified exosomes, protein concentrations were determined using the BCA assay kit (Beyotime, Beijing, China). Equal amounts (50 μg) of exosome samples were identified by immunoblot analysis using canonical exosomal markers CD63 and TSG101 after purification from TECs. The exosomes were diluted using 1 × PBS buffer to 5 μg/mL for nanoparticle tracking analysis (NTA). Particle concentration and size distribution were measured using Zetaview-PMX120-Z (Particle Metrix, NRW, German). During the procedure, temperature was maintained around 23 and 30 °C. Morphological analysis (TEM) was performed using JEM1400 transmission electron microscope (JEOL, Tokyo, Japan). The resuspended exosomes were negative staining with 2% phosphotungstic acid (PTA) for 3 min and imaging *via* transmission electron microscope. Both NTA and TEM analyses were conducted by BioMISP (Wuhan, China).

The exosomes from the extracellular space of mice kidney were isolated as previously described[23]. Fresh mice kidney was dissected, washed with 1 × PBS and treated with Collagenase D (Roche, Basel, Switzerland), for 20 min at 37 °C. The dissociated tissue was filtered through a 40-μm mesh filter. Then the filtrate was centrifuged following the same steps as well as cellular supernatant to isolated the exosome pellet. The collected exosome pellet was resuspended in 2 mL of 0.95 mol/L sucrose solution and inserted inside a sucrose step gradient column as previously described[23]. The sucrose step gradient was centrifuged at 200,000×*g* for 16 h at 4 °C. The fractions on the top of the gradient were collected and centrifugation at 100,000×*g* for 70 min at 4 °C. Finally, the exosome pellet was resuspended in 1 × PBS or lysis buffer for further analysis.

2.12. Dil-C18 labeling of exosome

HK-2 cells were labeled with cell membrane fluorescent probe Dil-C18 (Yeasen, Shanghai, China) with a final concentration of 5 μmol/L for 1 h. After the treatment, the medium was aspirated, and the cells were washed three times with 1 × PBS and then incubated with fresh serum-free medium for additional 48 h. Finally, the CM of Dil-labeled HK-2 cells were collected to treat NRK-49F.

2.13. RNA stability assay

RNA stability assay was performed as previously reported[24]. HK-2 cells were collected at different time points after incubated with

kidneys from sham mice (n = 5) and UUO mice with or without TGF-β inhibition (n = 5). (H) The immunoblot analysis of phosphorylated Smad3 and NAT10 was performed in kidneys from sham mice (n = 3) and UUO mice with or without TGF-β inhibition (n = 5). (I) The immunofluorescence staining of NAT10 was performed in kidneys with indicated treatment. (J) The qRT-PCR analysis of NAT10 was performed in HK-2 cells with indicated treatment (n = 3). (K) The immunoblot analysis of *p*-Smad3 and NAT10 were performed in HK-2 cells with indicated treatment. (L) The Ch-IP analysis with Smad3 antibody was performed in HK-2 cells with or without TGF-β treatment (n = 3). (M) The graph indicating the mutation strategy in NAT10 promoter. (N) The luciferase reporter analysis of NAT10 promoter was performed in 293T cells (n = 3). (O) The analysis of relationship between Smad3 expression and NAT10 expression was performed in human kidneys *via* GEPIA Database. Data are presented as mean ± SD. One-way ANOVA or two-way ANOVA was used for comparison between multiple groups; *P < 0.05; **P < 0.01; ***P < 0.001.

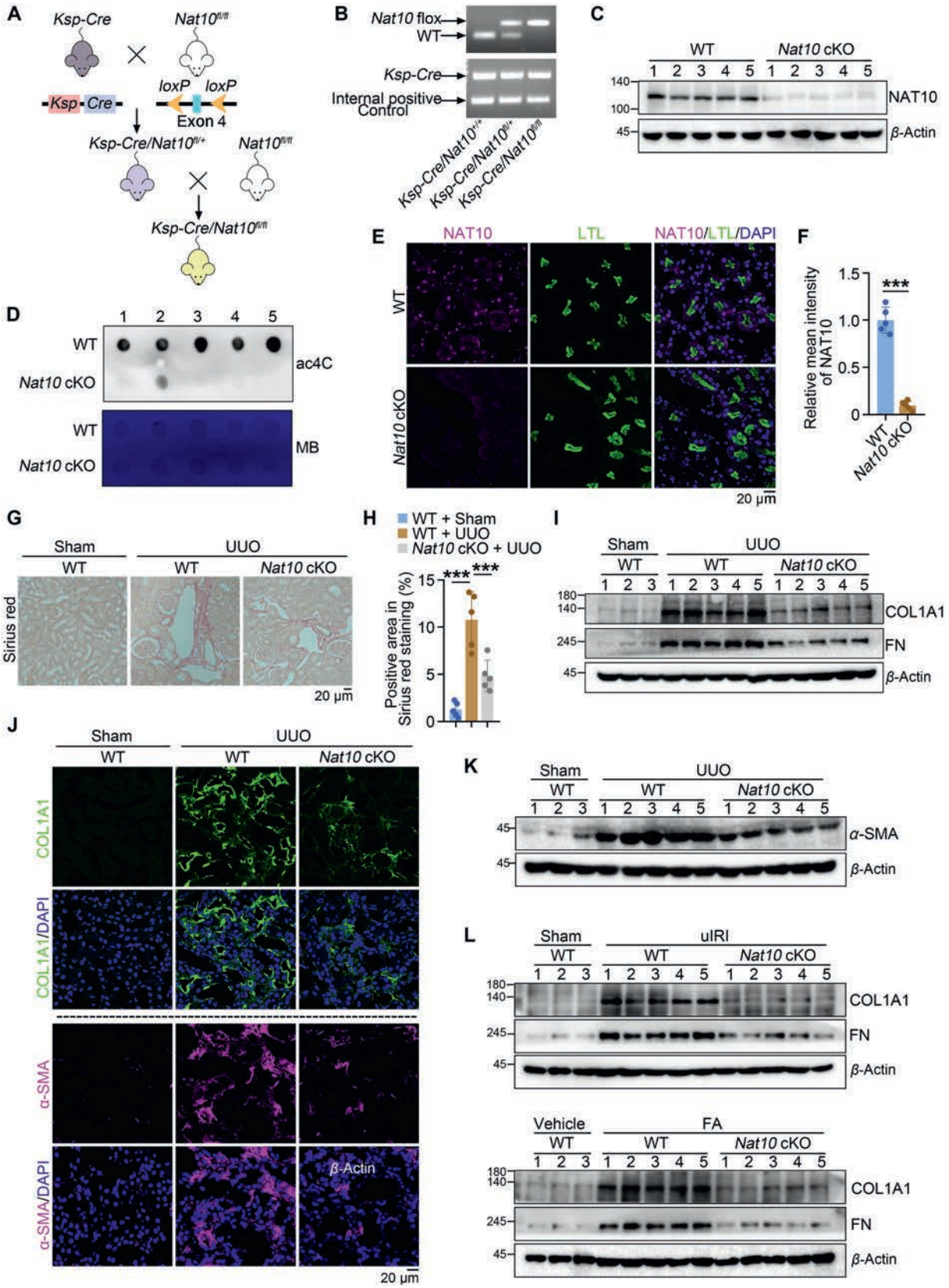

Figure 3 Conditional knockout of NAT10 alleviates renal fibrosis *in vivo*. (A) The graph indicating the strategy of constructing *Nat10*-cKO mice. (B) The PCR analysis of *Nat10* was performed in the kidneys from wild-type and *Nat10*-cKO mice. (C) The immunoblot analysis of NAT10 was performed in the kidneys from wild-type ($n = 5$) and *Nat10*-cKO mice ($n = 5$). (D) The dot blot analysis of ac4C was performed in the kidneys from wild-type ($n = 5$) and *Nat10*-cKO mice ($n = 5$). (E, F) The immunofluorescence staining of NAT10 was performed (E) and

actinomycin D (5 μg/mL) and the total RNA was isolated for qRT-PCR to analyze the mRNA levels of targeted genes.

2.14. $NaBH_4$ treatment and Sanger Sequencing

$NaBH_4$ treatment was performed as previously reported[24]. Total RNA was isolated from HK-2 cells using TRIzol reagent. Then, 2 μg RNA was treated with $NaBH_4$ with a final concentration of 100 mmol/L. $NaBH_4$-treated RNA samples were incubated at 37 °C for 1 h, and $NaBH_4$ was then quenched with 1 mol/L HCl (15 μL) and neutralized by 1 mol/L Tris−HCl (pH 8.0) buffer (15 μL). Sanger Sequencing was performed by the Sangon Biotech Company (Shanghai, China).

2.15. GTP-agarose pull-down assay

To detect the activity of Rab11a, the GTP-agarose beads (Sigma, MO, USA) were used. Briefly, the cells were homogenized with cell lysis buffer and then centrifuged at 12,000×*g* for 20 min at 4 °C. The GTP-agarose beads were washed three times with lysis buffer and equivalent amounts of cell lysates were added. After incubating overnight at 4 °C, the GTP-agarose beads were washed five times with cell lysis buffer and SDS loading buffer was added. After boiling for 10 min, the samples were separated by polyacrylamide gel electrophoresis using a Mini PROTEAN® Tetra Cell western system (Bio-Rad, CA, USA) and transferred to PVDF membranes. Finally, the abundance of GTP-bound or total Rab11a was measured by immunoblot with specific antibody of Rab11a.

2.16. Animal experiments

Tubular *Nat10* conditional knockout mice were established by mating *Nat10* floxed mice with *Ksp*-Cre transgenic mice. *Nat10* floxed mice and *Ksp*-Cre transgenic mice were in C57BL/6 background and purchased from Cyagen Bioscience (Guangzhou, China).

Unilateral ureteral obstruction (UUO), unilateral ischemia/reperfusion injury (uIRI) and folic acid (FA, Sigma, MO, USA) nephropathy were used to establish *in vivo* models of renal fibrogenesis[25]. Briefly, 8-week-old C57BL/6 male mice were used and randomly divided into groups (at least 3 mice per group). For UUO model, mice were anesthetized and placed on a homeothermic table. Midline incision was made and the left ureter was ligated, and 7 days later, mice were sacrificed and the kidneys were collected. For uIRI model, the left renal pedicle was clamped for 30 min, and 11 days later mice were sacrificed and the kidneys were collected. For FA model, 250 mg/kg folic acid was injected intraperitoneally into mice, and 14 days later mice were sacrificed and the kidneys were collected.

To investigate the effect of Remodelin *in vivo*, Remodelin (10 mg/kg) was injected intraperitoneally in mice with or without UUO/uIRI/FA treatment.

Serum creatinine and BUN levels were measured using serum creatinine (Scr) and blood urea nitrogen (BUN) detection kits (Nanjing Jiancheng, Nanjing, China). Both measurements were performed according to the manufacturers' instructions.

2.17. Luciferase reporter assay

The wild-type and mutant promoter of NAT10 (−2380 to −2389) was constructed into pGL3-enhancer vector. The HEK293T cells transfected respectively with wild-type NAT10 promoter plasmid or mutant NAT10 promoter plasmid, were treated with or without TGF-β (5 ng/mL) for 24 h. Next, the luciferase activities were quantified with Dual-luciferase Reporter Assay Kit (Promega, WI, USA) according to manufacturer's protocol.

2.18. Statistical analysis

In each experiment, data are presented as the mean ± standard deviation (SD). Student's *t* test was used to analysis the statistical significance for two groups and one-way ANOVA with Tukey multiple comparisons test was used for multiple groups. Two-way ANOVA with Tukey multiple comparisons test was used to analysis data with two variables. Effect sizes were reported as Cohen's with 95% confidence intervals. The pearson correlation test was used to analysis the correlation. Data were performed with GraphPad Prism 8.0.

3. Results

3.1. Targeting acetyltransferase NAT10 with remodelin breaks the pro-fibrotic TEC-fibroblast chain

As the main cause of renal fibrosis, fibroblast activation is activated by TEC-derived exosomes, whose secretion is stimulated by TGF-β[4,26]. To investigate how to break activating axis of fibroblast, an *in vitro* model was constructed for high-throughout screen (Fig. 1A). Epigenetic targeting now is the leading strategy in drug discovery[27], therefore, epigenetic compound library (TargetMol) was utilized for screen. 416 inhibitors (5 μmol/L each) were used to treat TGF-β-stimulated HK-2 cells and the conditioned media (CM) were collected to treat NRK-49F fibroblasts. As demonstrated by CCK8 assays, 37 inhibitors were effective in suppressing proliferation of NRK-49F cells in both 24 and 48 h compared to the control (dimethyl sulfoxide, DMSO) (Fig. 1B). The inhibitors displaying significantly different effects between duplicates were excluded. Next, the selected inhibitors were applied for further screen with a lower concentration

analyzed (F) in the kidneys from wild-type and *Nat10*-cKO mice. (G, H) The Sirius Red analysis was performed (G) and analyzed (H) in the kidneys from sham mice ($n = 5$) and UUO mice ($n = 5$) with or without condition *Nat10* knockout. (I) The immunoblot analysis of collagen I and fibronectin was performed in the kidneys from sham mice ($n = 3$) and UUO mice ($n = 5$) with or without condition *Nat10* knockout. (J) The immunofluorescence staining of collagen I and α-SMA were performed in the kidneys from sham mice ($n = 5$) and UUO mice ($n = 5$) with or without conditional *Nat10* knockout. (K) The immunoblot analysis of α-SMA was performed in kidneys from sham mice ($n = 3$) and UUO mice ($n = 5$) with or without condition *Nat10* knockout. (L) The immunoblot analysis of collagen I and fibronectin was performed in kidneys from sham mice ($n = 3$) and uIRI/FA mice ($n = 5$) with or without condition *Nat10* knockout. Data are presented as mean ± SD. Student's *t* test was used for comparison between two groups and one-way ANOVA was used for comparison between multiple groups; $^*P < 0.05$; $^{**}P < 0.01$; $^{***}P < 0.001$.

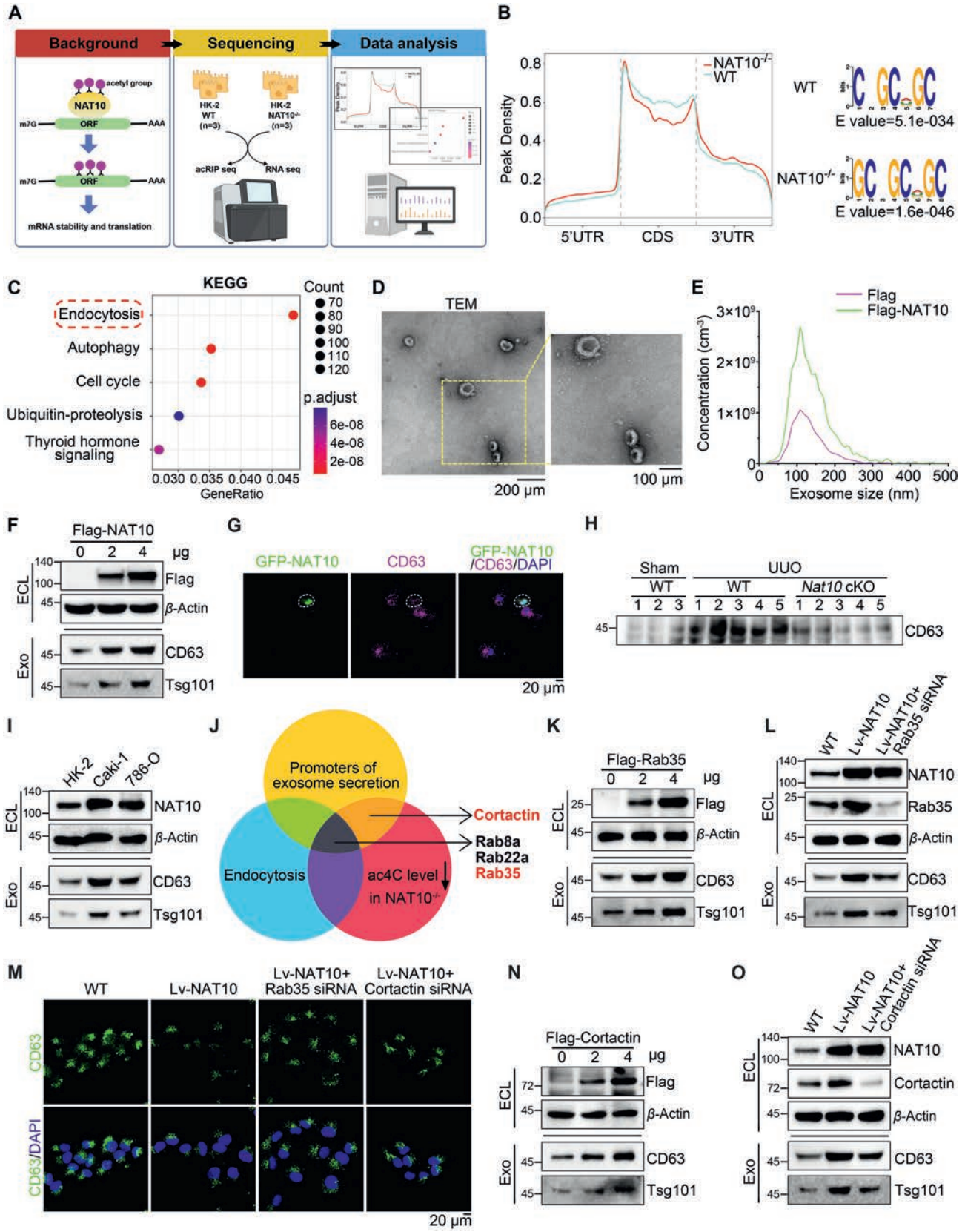

Figure 4 NAT10-ac4C axis promotes secretion of exosome in TEC through Rab35 and Cortactin. (A) The graph demonstrating the workflow of analyzing the downstream genes of NAT10−ac4C axis in TEC. (B) The graph demonstrating the ac4C peaks (left) and the canonical ac4C motifs (right) in wild-type HK-2 cells and NAT10-depleted HK-2 cells. (C) The graph demonstrating the KEGG analysis of potential downstream genes of NAT10−ac4C axis. (D) The representative transmission electron microscopic image of exosome isolated from HK-2 cells. (E) The representative

(1 μmol/L each), and 13 of them were still effective in both 24 and 48 h (Fig. 1C and D).

We next clinically analyzed whether the targets (Fig. 1D) of these compounds were promising targets for renal fibrosis depending on the Nephroseq Database (https://nephroseq.org). The glomerular filtration rate (GFR) below 60 mL/min is the standard characteristic of CKD. Multiple candidates showed higher expression in patients whose GFRs are below 60 mL/min (Supporting Information Fig. S1A), and some of them were already reported to participate in renal fibrosis such as HDAC1 and HDAC2. The acetyltransferase NAT10 caught our attention because we previously focused on NAT10's roles in carcinogenesis[16,17]. The level of NAT10 is negatively associated with the GFRs of patients (Fig. S1B). We further confirmed that NAT10 silencing in TEC attenuated TGF-β-CM-induced fibroblast activation (Fig. S1C), confirming NAT10 targeting disrupted TEC-fibroblast chain.

We next examined NAT10 expression in canonical *in vivo* models of renal fibrosis including unilateral ureteral obstruction (UUO), ischemia−reperfusion injury (uIRI) and folic acid (FA) administration[25,28]. Elevated NAT10 levels were found in all models (Fig. 1E, Fig. S1D and S1E). Given NAT10 as the only writer of ac4C modification, we next tested the ac4C levels and found increased ac4C levels in fibrotic kidneys (Fig. 1F, Fig. S1F and S1G). Furthermore, immunohistochemistry (IHC) staining supported NAT10 upregulation in UUO model (Fig. 1G). Interestingly, besides the nuclear NAT10, the cytoplasmic NAT10 was also upregulated in fibrotic kidney. As indicated by the co-staining with proximal tubular cell marker LTL, NAT10 was mainly expressed in TEC (Fig. 1H, Fig. S1H and S1I). Analysis of single-cell RNA-seq supported that NAT10 was mainly expressed in proximal tubular cells (Fig. S1J). Finally, we collected kidney tissues from 5 patients without CKD as non-CKD control and 18 patients previously diagnosed as CKD. Compared to non-CKD tissues, NAT10 expression and ac4C levels were both increased in CKD tissues (Fig. 1I and J).

3.2. TGF-β-Smad3 signaling is responsible for NAT10 upregulation in TEC during renal fibrogenesis

How NAT10−ac4C axis was upregulated in TEC during renal fibrogenesis was investigated. Among canonical pro-fibrotic pathways, TGF-β−Smad3 signaling is the dominant one[29]. Motif analysis of NAT10 promoter with JASPR Database identified a canonical Smad3-binding motif in NAT10 promoter (Fig. 2A), suggesting NAT10 as a potential target of TGF-β−Smad3 signaling. Furthermore, TGF-β treatment elevated both mRNA and protein levels of NAT10 in HK-2 cells (Fig. 2B−D). According to GEPIA Database (http://gepia.cancer-pku.cn/), TGF-β expression is positively correlated with NAT10 expression in human kidneys (Fig. 2E). The ac4C level was also enhanced following TGF-β treatment (Fig. 2F). Next, we treated the UUO mice with TGF-β inhibitor SB431542 and found an attenuated NAT10 upregulation i n kidneys (Fig. 2G−I), indicating TGF-β as one of main stimulators of NAT10 expression during renal fibrogenesis. Next, whether TGF-β upregulated NAT10 *via* Smad3 was investigated. HK-2 cells were treated with Smad3 inhibitor SIS3 after TGF-β treatment. Smad3 inhibition buffered TGF-β′s effect on NAT10 (Fig. 2J and K). Next, chromatin immunoprecipitation (Ch-IP) was performed, demonstrating that Smad3 bound to NAT10 promoter (Fig. 2L). Meanwhile, the wild-type and mutant promoter of NAT10 was constructed into pGL3-enhancer vector (Fig. 2M), and the luciferase reporter assay was performed. TGF-β almost failed to activate the transcription of mutant NAT10 promoter (Fig. 2N), validating that TGF-β−Smad3 signaling stimulated NAT10 transcription in TEC. GEPIA database indicated that Smad3 expression positively correlates with NAT10 expression in human kidneys (Fig. 2O).

3.3. Conditional knockout of NAT10 alleviates renal fibrosis in vivo

To gain a reliable insight into NAT10's role in renal fibrosis, we generated renal tubule-specific *Nat10* conditional knockout (cKO) mice (Fig. 3A). The expression of *Nat10* was examined by tail genotyping (Fig. 3B), immunoblot (Fig. 3C, Supporting Information Fig. S2A) and immunofluorescence staining (Fig. 3E and F). Besides, ac4C level in *Nat10*-cKO mice was much decreased (Fig. 3D), indicating efficient suppression of NAT10−ac4C axis in *Nat10*-cKO mice. Next, UUO was performed with wild-type and *Nat10*-cKO mice. Sirius Red staining showed that the kidneys of *Nat10*-cKO mice was less fibrotic (Fig. 3G and H). Immunoblots and immunofluorescence staining showed that ECM accumulation and fibroblast activation in kidneys following UUO were mitigated by *Nat10* knockout (Fig. 3I−K, Fig. S2B). Similar findings that the elevated ECM production in kidneys was milder in *Nat10*-cKO mice, were also found in uIRI and FA models (Fig. 3L). These *in vivo* data illustrated NAT10 as a pro-fibrotic role in kidney.

NTA analysis of EVs isolated from wild-type HK-2 cells and NAT10-overexpressed HK-2 cells. (F) The immunoblot analysis of Flag-NAT10, CD63 and TSG101 was performed in HK-2 cells transfected with Flag-NAT10 or in exosomes isolated from equal numbers of cells. (G) The immunofluorescence staining of CD63 was performed in HK-2 cells transfected with GFP-NAT10. (H) The immunoblot analysis of CD63 was performed in Sucrose step gradient fractions isolated from the extracellular space from sham mice ($n = 3$) and UUO mice ($n = 5$) with or without condition *Nat10* knockout. (I) The immunoblot analysis of NAT10, CD63 and TSG101 was performed in HK-2, Caki-1 and 786-O cells or in exosomes isolated from equal numbers of cells. (J) The Venn diagram demonstrating the genes which favor exosome secretion among the potential downstream genes of NAT10−ac4C axis. (K) The immunoblot analysis of Flag-Rab35, CD63 and TSG101 was performed in HK-2 cells transfected with Flag-Rab35 or in exosomes isolated from equal numbers of cells. (L) The immunoblot analysis of NAT10, Rab35, CD63 and TSG101 was performed in HK-2 cells with indicated treatment or in exosomes isolated from equal numbers of cells. (M) The immunofluorescence staining of CD63 was performed in HK-2 cells with indicated treatment. (N) The immunoblot analysis of Flag-Cortactin, CD63 and TSG101 was performed in HK-2 cells transfected with Flag-Cortactin or in exosomes isolated from equal numbers of cells. (O) The immunoblot analysis of NAT10, Cortactin, CD63 and TSG101 was performed in HK-2 cells with indicated treatment or in exosomes isolated from equal numbers of cells.

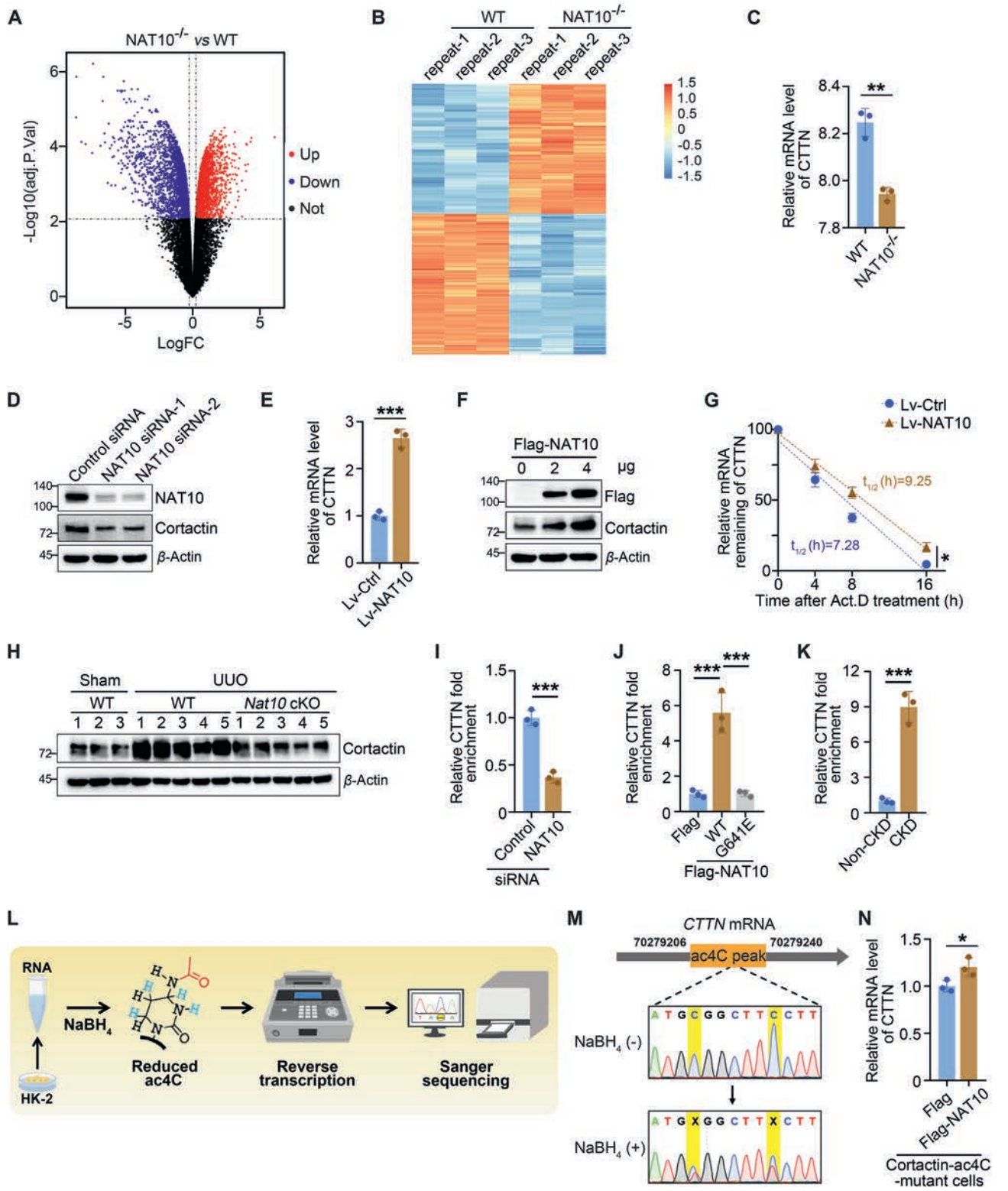

Figure 5 NAT10−ac4C axis upregulates Cortactin *via* mRNA stabilization. (A) The volcano graph demonstrating the deferentially expressed genes between wild-type HK-2 cells ($n = 3$) and NAT10-depleted HK-2 cells ($n = 3$). (B) The heatmap demonstrates the differentially expressed genes between wild-type HK-2 cells ($n = 3$) and NAT10-depleted HK-2 cells ($n = 3$). (C) The mRNA level of Cortactin in wild-type and NAT10-depleted HK-2 cells was analyzed using RNA sequencing. (D) The immunoblot analysis of NAT10 and cortactin was performed in HK-2 cells with or without NAT10 silencing. (E) The qRT-PCR analysis of Cortactin was performed in wild-type ($n = 3$) and NAT10-stably-expressed HK-2 cells ($n = 3$). (F) The immunoblot analysis of Cortactin was performed in wild-type and NAT10-stably-expressed HK-2 cells. (G) The mRNA half-life analysis of cortactin was performed in in control ($n = 3$) and NAT10-stably-expressed HK-2 cells ($n = 3$). (H) The immunoblot analysis of Cortactin was performed in kidneys from sham mice ($n = 3$) and UUO mice ($n = 5$) with or without conditional *Nat10* knockout.

3.4. NAT10−ac4C axis promotes secretion of exosomes from TEC through Rab35 and cortactin

We next investigated how NAT10 promoted renal fibrosis. Considering NAT10 as the only writer of mRNA ac4C modification, we first explored the downstream genes of NAT10−ac4C axis in TEC. To this end, wild-type (WT) and NAT10-depleted HK-2 cells were used for ac4C RNA immunoprecipitation sequencing (acRIP-seq) (Fig. 4A). We confirmed that NAT10 depletion impaired ac4C modification (Fig. 4B, left panel), mainly in the coding sequence (CDS). Motif analysis indicated the canonical ac4C motif (CXXCXX) as the top ac4C peaks in both cells (Fig. 4B, right panel). The genes whose ac4C levels were down-regulated in NAT10-depleted cells were considered as potential target genes of NAT10−ac4C axis. KEGG analysis indicated that many of them were enriched in endocytosis, which is closely associated with biogenesis and secretion of exosome (Fig. 4C). Exosome is the main mediator of cell−cell communication, especially in the TEC-fibroblast chain. Overactivated exosome secretion of TEC is the both the characteristic and the driver of renal fibrogenesis[4,26]. These evidences together implied us that NAT10's pro-fibrotic effect may depend on exosome. Next, the extracellular vesicles (EVs) were isolated from identical amounts of control HK-2 cells and NAT10-stably-transfected HK-2 cells. Transmission electron microscopy (TEM) proved that the EVs isolated from HK-2 cells were mainly exosomes (Fig. 4D). Nanoparticle tracking analysis (NTA) showed that the concentration of EVs from NAT10-overexpressed HK-2 cells was higher than that from control cells (Fig. 4E), suggesting that NAT10 favored exosome secretion of TEC. To confirm this finding, we transfected HK-2 cells with Flag-NAT10 and isolated the exosomes. Immunoblots showed that NAT10 elevated the quantity of HK-2-derived exosomes depending on its acetyltransferase activity, as indicated by the exosome markers CD63 and TSG101 (Fig. 4F and Supporting Information Fig. S3A). The intracellular accumulation of CD63 is the characteristic of impaired exosome secretion[23,30]. As demonstrated by immunofluorescence staining, less CD63 accumulation was found in NAT10-overexpressed HK-2 cells (Fig. 4G, Fig. S3B and S3C), proving that NAT10 favored exosome secretion of TEC. On the contrary, after isolating the exosomes from the extracellular space of kidney from WT and *Nat10*-cKO mice with or without UUO, we found that the exosomes in extracellular space of kidneys were increased by UUO treatment, which was reversed in *Nat10*-cKO mice (Fig. 4H). Therefore, the positive relationship between NAT10 and exosome secretion was validated *in vivo*. The clear cell renal cell cancer (ccRCC) is malignantly transformed from TEC. We found that compared to HK-2 cells, NAT10 expression and the quantity of exosomes were both higher in ccRCC cells (Fig. 4I). Further, NAT10 silencing in Caki-1 cells inhibited exosome release (Fig. S3D).

We next went deeper into how NAT10 promoted exosome secretion. The secretion of exosome is mainly regulated by Rab GTPases family, SNARE family and cytoskeleton regulators[31]. We found several Rab members in the above endocytosis-related genes. Among them, Rab8a[32], Rab22a[33] and Rab35[34] were previously reported to facilitate exosome secretion (Fig. 4J), suggesting that NAT10−ac4C axis might function through them. Considering these Rab members had not been reported in kidney, we transfected Flag-Rab8a, Flag-Rab22a or Flag-Rab35 in HK-2 cells and the exosomes were isolated from the same amounts of these cells. Enhanced exosome secretion was only observed in Rab35-transfected HK-2 cells (Fig. 4K, Supporting Information Fig. S3E and S3F). Conversely, Rab35 knockdown inhibited exosome secretion (Fig. S3G), illustrating that Rab35 functioned in TEC. More importantly, the elevated exosome release of NAT10-stably-expressed HK-2 cells were partly relieved by Rab35 silencing (Fig. 4L and M), indicating that NAT10−Rab35 axis promoted exosome secretion in TEC.

Besides Rabs, cytoskeleton regulators are also indispensable regulators of exosome secretion, including Rho family, ERM protein, Arp complex and Cortactin[31]. Among these regulators, Cortactin, the cooperator of Rab35 and Rab27a in determining exosome secretion[35,36], was also potentially regulated by NAT10−ac4C axis (Fig. 4J and Fig. S3J). After validating that Cortactin was functional in TEC (Fig. 4N and Fig. S3H), we found Cortactin as another mediator of NAT10 to favor exosome release (Fig. 4O). We next found that Rab35 and Cortactin were both upregulated in UUO, uIRI and FA models (Fig. S3I), supporting that NAT10 may upregulate Rab35 and Cortactin to promote exosome secretion during renal fibrogenesis.

3.5. NAT10-ac4C axis upregulates cortactin via mRNA stabilization

Therefore, whether NAT10−ac4C axis upregulated Rab35 and Cortactin was investigated. Thus, RNA-seq was performed with WT and NAT10-depleted HK-2 cells. A large number of genes were identified differentially expressed in response to NAT10 depletion, especially the downregulated ones (Fig. 5A and B). Unexpectedly, a mild increase rather than a decrease of Rab35 mRNA was detected in NAT10-dpleted HK-2 cells (Supporting Information Fig. S5A). Unlike Rab35, Cortactin expression was impaired by NAT10 depletion (Fig. 5C and D). Moreover, we confirmed that NAT10 upregulated Cortactin depending on ac4C (Fig. 5E and F, Supporting Information Fig. S4A). NAT10 expression was positively associated with Cortactin expression in healthy human kidneys and CKD kidneys (Fig. S4B and S4C). Previous studies indicated that NAT10−ac4C axis functioned *via* mRNA stabilization. Therefore, mRNA half-life assay was performed, demonstrating that *Cortactin* decay was decelerated in NAT10-stably-expressed HK-2 cells (Fig. 5G), indicating that NAT10 stabilized *Cortactin*. Moreover, Cortactin upregulation following UUO was evidently alleviated in *Nat10*-cKO mice (Fig. 5H), demonstrating the NAT10−ac4C−Cortactin cascade in renal fibrosis.

The acRIP-seq identified an ac4C peak on *Cortactin* (Fig. S3J), and it was validated by acRIP-qRT-PCR (Fig. 5I and J). Meanwhile, an increased level of ac4C-modified *Cortactin* was found in

(I) The acRIP-qRT-PCR analysis of Cortactin in HK-2 cells with or without NAT10 silencing ($n = 3$). (J) The acRIP-qRT-PCR analysis of Cortactin in HK-2 cells with or without transfection of wild-type or mutant NAT10 ($n = 3$). (K) The acRIP-qRT-PCR analysis of Cortactin in kidneys from CKD patients and non-CKD control. (L) The graph indicating the procedure of RedaC:T-Sanger-seq. (M) The RedaC:T-Sanger-seq analysis of Cortactin ac4C peak in HK-2 cells. (N) The qRT-PCR analysis of Cortactin in Cortactin-ac4C-mutant HK-2 cells with or without NAT10 transfection ($n = 3$). Data are presented as mean ± SD. Student's t test was used for comparison between two groups and one-way ANOVA was used for comparison between multiple groups; $^{*}P < 0.05$; $^{**}P < 0.01$; $^{***}P < 0.001$.

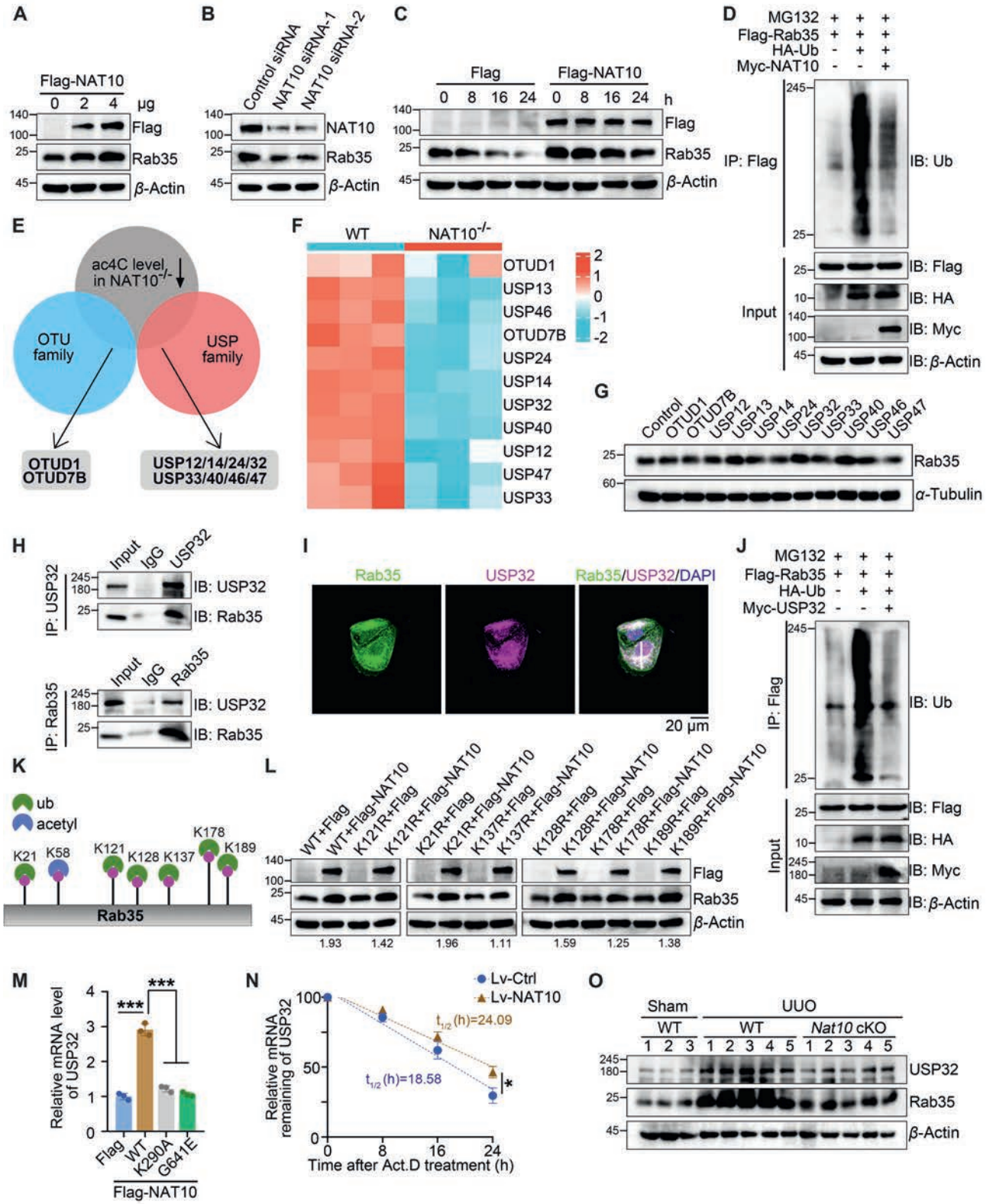

Figure 6 NAT10−ac4C axis enhances stabilizes Rab35 protein *via* USP32-mediated deubiquitination. (A) The immunoblot analysis of Rab35 and Flag-NAT10 in HK-2 cells transfected with Flag-NAT10. (B) The immunoblot analysis of Rab35 and NAT10 in HK-2 cells with or without NAT10 silencing. (C) The protein half-life analysis of Rab35 in HK-2 cells transfected with Flag-NAT10. (D) The immunoblot analysis of Rab35 ubiquitination in HK-2 cells with indicated treatment. (E) The Venn diagram demonstrates the deubiquitinases among the potential downstream genes of NAT10−ac4C axis. (F) The heatmap demonstrating the expression profile of indicated deubiquitinases in wild-type ($n = 3$) and NAT10-depleted HK-2 cells ($n = 3$). (G) The immunoblot analysis of Rab35 was performed in HK-2 cells transfected with the indicated plasmids, respectively.

CKD tissues (Fig. 5K). To specify the ac4C site on *Cortactin*, RedaC:T-Sanger-seq was performed in HK-2 cells with or without $NaBH_4$ treatment (Fig. 5L), displaying two ac4C sites in the peak (Fig. 5M). Mutation of these ac4C sites impaired *Cortactin* stability (Fig. S4E). In the ac4C-mutant HK-2 cells, NAT10 almost lost its effect on Cortactin (Fig. 5N).

3.6. NAT10 enhances protein level of Rab35 via USP32-mediated deubiquitination

Although NAT10 did not increase Rab35 mRNA, the proved NAT10−Rab35 axis still drove us to suspect whether NAT10 regulated protein level or activity of Rab35. Surprisingly, NAT10 overexpression or knockdown significantly increased or decreased the protein level of Rab35 (Fig. 6A and B), suggesting that NAT10 upregulated Rab35 translationally or post-translationally. Although ac4C may promote translation efficiency, the finding that NAT10 downregulated Rab35 mRNA suggested that NAT10 was unlikely to enhance translational efficiency of Rab35. We thus performed protein half-life assay and found that Rab35 degradation was milder in Flag-NAT10-transfected HK-2 cells (Fig. 6C), indicating that NAT10 stabilized Rab35 protein. The ubiquitination-deubiquitination homeostasis dominates protein stability, we thus suspected whether NAT10 affected Rab35 ubiquitination. In Flag-Rab35-transfected HK-2 cells with or without co-transfection of HA-ubiquitin, the immunoprecipitation was performed with anti-Flag, and the further immunoblot was performed with anti-HA antibody. A prominent increase of Rab35 ubiquitination was observed in HK-2 cells co-transfected with Flag-Rab35 and HA-ubiquitin (Fig. 6D). Additional transfection of Myc-NAT10 reduced Rab35 ubiquitination (Fig. 6D), indicating that NAT10 promoted Rab35 deubiquitination.

Considering NAT10 does not encode any protein with deubiquitinase activity, we hypothesized that NAT10 affected Rab35 through certain deubiquitinase. Combined analysis of acRIP-seq and RNA-seq uncovered a number of canonical deubiquitinases as potential downstream targets of NAT10−ac4C axis (Fig. 6E and F). We next transfected HK-2 cells with each of these deubiquitinases and found that transfection of USP13, USP32 or USP40 elevated Rab35 protein (Fig. 6G). Furthermore, USP32 silencing displayed the most significant effect in repressing Rab35 (Fig. S5B and S5C), implying USP32 as a negative regulator of Rab35. Next, co-immunoprecipitation and immunofluorescence staining were performed (Fig. 6H and I, Fig. S5D), demonstrating the interaction between USP32 and Rab35. More importantly, we found that USP32 transfection decreased Rab35 ubiquitination (Fig. 6J), supporting USP32 as the deubiquitinase of Rab35.

According to the Phosphosite Database (https://www.phosphosite.org/), K21, K121, K128, K137, K178 and K189 are proved ubiquitination sites of Rab35 (Fig. 6K). We next examined which lysine mediated NAT10 to upregulate Rab35. Rab35 K21R-, K121R-, K128R-, K137R-, K178R- or K189R-mutant HK-2 cells were constructed, and Flag-NAT10 was transfected in each of these cells respectively. Compared with wild-type HK-2 cells, NAT10 only displayed subtle effects on Rab35 in K137R-mutant and K178R-mutant cells (Fig. 6L), indicating that NAT10 mainly functioned through K137 and K178 of Rab35. Furthermore, we confirmed that NAT10 elevated USP32 *via* stabilizing its mRNA (Fig. 6M and N). More than that, the elevation of USP32 and Rab35 induced by UUO was suppressed in *Nat10*-cKO mice (Fig. 6O). The positive association between NAT10 expression and USP32 expression was validated in healthy human kidneys and CKD kidneys (Fig. S5E and S5F). We next validated the ac4C peak in *USP32* (Fig. S5G−S5I), and found more ac4C-modified *USP32* in CKD tissues (Fig. S5J). Two ac4C sites were identified by RedaC:T-Sanger-seq among ac4C peak, and after mutating these ac4C sites NAT10 was only able to show a diluted effect on Cortactin (Fig. S5K and S5L). Finally, we found that USP32 ablation broke NAT10−Rab35 regulatory axis (Fig. S5M).

3.7. The cytoplasmic NAT10 contributes to exosome secretion of TEC via acetylating and activating Rab11a

Although previous studies involving NAT10 rarely turned an eye to the other subcellular fractions of NAT10, we noticed that the cytoplasmic NAT10 was also upregulated in fibrotic kidneys (Fig. 1G and H). We thus examined NAT10 abundance in nucleus and cytoplasm of CKD tissues, and found that NAT10 was expressed more or less in the cytoplasm of CKD tissues (Fig. 7A), intriguing us to wonder whether the cytoplasmic NAT10 played a role. In order to drive NAT10 out of nucleus, the nuclear localization sequence (NLS) of NAT10 which was previously identified[17] was deleted in HK-2 cells (NAT10-ΔNLS). Next, the wild-type, NAT10-deleted and NAT10-ΔNLS HK-2 cells were treated with TGF-β respectively, and the CM were collected to incubate NRK-49F cells (Fig. 7B). Surprisingly, the CM from NAT10-ΔNLS cells still displayed an impaired effect on fibroblast activation (Fig. 7C and D). These results indicated that besides the nuclear fraction, the cytoplasmic NAT10 also functioned in TEC-fibroblast chain.

Besides ac4C modification which makes a difference mainly in nucleus, NAT10 is also an acetyltransferase catalyzing Kac in all subcellular compartments. Therefore, we suspected NAT10 functioned in TEC-fibroblast chain *via* protein acetylation. We next screened the protein binding profile of NAT10 *via* the Biogrid Database (https://thebiogrid.org) to investigate whether NAT10 directly bound with exosome regulators. Surprisingly, Rab11a which was reported to promote exosome release[37], is its binding partner. Further, we confirmed that NAT10 bound to Rab11a in HK-2 cells depending on its N terminal domain (Fig. 7E and F, Supporting Information Fig. S6A). In comparison, no interaction between NAT10 and Cortactin or Rab35 was detected (Fig. 7E). Moreover, we confirmed that NAT10 favored Rab11a acetylation (Fig. 7G and H). As indicated by the co-staining of Flag-NAT10-

(H) The co-immunoprecipitation analysis with USP32 antibody (top) or Rab35 antibody (bottom) in HK-2 cells. (I) The immunofluorescence staining of Rab35 and USP32 were performed in HK-2 cells. (J) The immunoblot analysis of Rab35 ubiquitination in HK-2 cells with indicated treatment. (K) The graph demonstrating the lysine sites modified by ubiquitination in Rab35 protein. (L) The immunoblot analysis of Rab35 was performed in wild-type and indicated mutant HK-2 cells transfected with Flag-NAT10. (M) The qRT-PCR analysis of USP32 was performed in HK-2 cells transfected with wild-type or mutant Flag-NAT10 plasmid ($n = 3$). (N) The mRNA half-life analysis of USP32 was performed in wild-type ($n = 3$) and NAT10-stably-expressed HK-2 cells ($n = 3$). (O) The immunoblot analysis of USP32 and Rab35 was performed in kidneys from wild-type ($n = 3$) or *Nat10*-cKO mice ($n = 5$) with or without UUO treatment. Data are presented as mean ± SD. Student's *t* test was used for comparison between two groups and one-way ANOVA was used for comparison between multiple groups; $^{*}P < 0.05$; $^{**}P < 0.01$; $^{***}P < 0.001$.

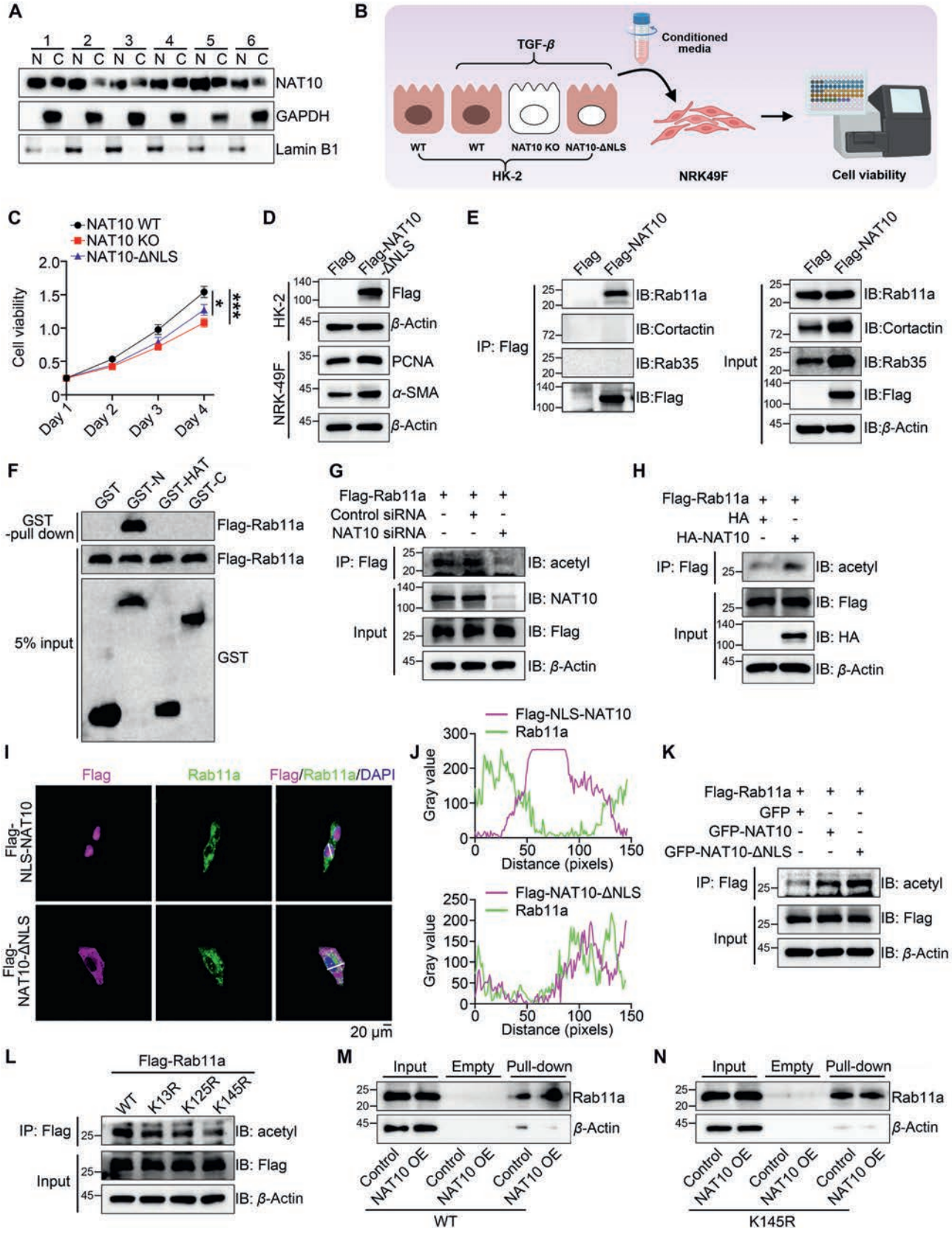

Figure 7 The cytoplasmic NAT10 also promotes exosome secretion *via* acetylating and activating Rab11a. (A) The immunoblot analysis of NAT10 the cytoplasm and nucleus of CKD tissues ($n = 6$). (B) The graph demonstrating the CM from indicated HK-2 cells which were used to treat NRK-49F cells. (C) The CCK8 analysis of NRK-49F cells ($n = 3$) treated with CM from indicated HK-2 cells. (D) The immunoblot analysis of PCNA and α-SMA in NRK-49F cells treated with CM from indicated HK-2 cells. (E) The Co-IP assay with anti-Flag antibody and immunoblot

ΔNLS and Rab11a, NAT10 mainly bound with Rab11a in the cytoplasm (Fig. 7I and J). NAT10-ΔNLS even induced Rab11a acetylation more significantly than NAT10 did (Fig. 7K). According to GPS-PAIL Database (http://bdmpail.biocuckoo.org), K13, K125 and K145 of Rab11a are potentially acetylated (Fig. S6B). Mutation of the K145 which is conserved across main species (Fig. S6C), substantially abolished NAT10-mediated Rab11a acetylation (Fig. 7L). The Rab members including Rab11a function *via* conversion between the GDP-bound state which is inactive and the GTP-bound state which is active[38]. Given that NAT10 showed no significant effect on Rab11a abundance, we thus investigated whether NAT10 affected Rab11a activation. As showed by GTP-agarose pull-down assay, NAT10 obviously increase the abundance GTP-bound state of Rab11a in WT HK-2 cells, which was lost in Rab11a K145R-mutant cells (Fig. 7M and N). These results indicated that the cytoplasmic NAT10 acetylated and induced Rab11a activation in TEC, supporting exosome secretion of TEC.

3.8. NAT10 upregulates the abundance of Gli2 and Gli1 in TEC-derived exosomes

TEC promotes fibroblast activation *via* exosomes[4]. We thus wondered whether NAT10 in TEC affected fibroblast *via* exosomes. The conditioned media (CM) collected from control or NAT10-stably-expressed HK-2 cells were used to treat NRK-49F cells (Fig. 8A). Co-staining of Dil and α-tubulin indicated that the HK-2-derived exosomes which were labeled with Dil-C18, were effectively absorbed by NRK-49F cells (Fig. 8B). First, we found that the CM from wild-type NAT10-overexpressed HK-2 cells activated NRK-49F cells (Fig. 8C−F and Supporting Information Fig. S7A). But this phenomenon almost disappeared after exosome removal (Fig. 8G), indicating that tubular NAT10 activated fibroblast mainly depending on exosomes.

Next, the same amounts of exosomes collected from control or NAT10-overexpressed (OE) cells were used to treat NRK-49F cells. The exosomes from NAT10-OE cells also activated NRK-49F cells (Fig. 8H), implying NAT10 functioned in fibroblast activation depending on not only exosome secretion, but also exosomal content. FGF2, PDGF, SHH and WNT are the most canonical triggers of fibroblast activation[39]. We thus investigated whether NAT10 affected this pro-fibrotic cargo *via* analyzing RNA-seq and acRIP-seq. We found that the FGF2 and members of SHH signaling including Gli1, Gli2 and Ptch might be downstream targets by NAT10 (Fig. 8I and J, Fig. S7B and S7C). However, although the CM from HK-2 cells transfected with Flag-FGF2 activated fibroblast, exosome removal almost showed no effects (Fig. S7D), indicating FGF2 was not downstream exosomal mediator of NAT10. In terms of the members of SHH signaling, we validated that NAT10 upregulated Gli1 and Gli2 at most depending on ac4C modification (Fig. 8K and L). The elevated Ptch expression may be a consequence of Gli upregulation since Ptch is also a target of Gli[40]. More importantly, we found that the abundance of Gli1 and Gli2 was elevated in exosomes derived from NAT10-overexpressed HK-2 cells (Fig. 8M). Co-staining of CD63 and Gli1 or Gli2 in HK-2 cells supported that Gli1 and Gli2 were encapsulated in exosomes (Fig. 8N and O).

The acRIP-seq only indicated a decrease ac4C peak on Gli2 mRNA upon NAT10 depletion (Fig. S7E). We further validated that NAT10 determined the ac4C levels of Gli2 (Fig. S7F and S7G), and observed the elevated ac4C-modified *Gli2* in CKD tissues (Fig. S7H). Moreover, mutation of the ac4C site on *Gli2* which was verified by RedaC:T-Sanger-seq, greatly abolished NAT10's effect on Gli2 expression (Fig. S7I and S7J). NAT10 expression was positively associated with Gli2 expression in healthy and CKD kidneys (Fig. S7K and S7L). Gli1 was a transcriptional target of Gli2, and we found that NAT10 only induced a subtle increase of Gli1 following Gli2 silencing (Fig. S7M), indicating the NAT10−Gli2−Gli1 axis.

3.9. Exosomal Gli1/2 from TEC plays an indispensable role in fibroblast activation

Although the activation of SHH−Gli signaling in fibroblast is a canonical mechanism of fibroblast activation, the role of exosomal Gli1/2 from TEC in fibroblast activation remained unexplored. To this end, we transfected GFP-Gli2 in HK-2 cells (Fig. 9A), and collected the exosomes to treat NRK-49F cells. Immunoblot and immunofluorescence staining indicated the effective transfer of GFP-Gli2 into NRK-49F cells *via* exosomes (Fig. 9B−D). We found that NRK-49F cells were activated after treatment of exosomal Flag-Gli1 or Flag-Gli2 (Fig. 9E and F). To validate the importance of exosomal Gli1/2 in fibroblast activation, we further treated Gli1-KO or Gli2-KO NRK-49F cells with exosomal Flag-Gli1 or Flag-Gli2 (Fig. 9G). Surprisingly, the exosomal Gli1 or Gli2 was still functional in fibroblast activation even when the endogenous Gli1 or Gli2 was depleted (Fig. 9H and I), emphasizing the importance of tubular Gli1/2-exosome-fibroblast chain. Next, we tested whether Gli2 mediated NAT10's pro-fibrotic effect *via* exosomes. Therefore, NAT10 was overexpressed in HK-2 cells with or without Gli2 silencing, and the exosomes were collected from these cells to treat NRK-49F cells. As demonstrated in Fig. 9J−L, Gli2 silencing impaired the effects of NAT10-OE exosomes in activating NRK-49F cells. Taken together, the Gli, especially Gli2 derived from TEC is vital in fibroblast activation *via* exosome-mediated transfer, which also played an indispensable role in NAT10's effect in renal fibrogenesis.

analysis of Rab11a, Cortactin and Rab35 in HK-2 cells with or without Flag-NAT10 transfection. (F) The GST pull-down assay of GST-NAT10 with Rab11a. (G) The Co-IP assay with anti-Flag antibody and immunoblot analysis of Rab11a acetylation in HK-2 cells with or without NAT10 silencing. (H) The Co-IP assay with anti-Flag antibody and immunoblot analysis of Rab11a acetylation in HK-2 cells with or without NAT10 overexpression. (I, J) The immunofluorescence staining and quantitative analysis of colocalization of Rab11a and wild-type or mutated NAT10 in HK-2 cells. (K) The Co-IP assay with anti-Flag antibody and immunoblot analysis of Rab11a acetylation in HK-2 cells with or without wild-type or mutated NAT10 overexpression. (L) The Co-IP assay with anti-Flag antibody and immunoblot analysis of Rab11a acetylation in indicated mutant HK-2 cells with Flag-NAT10 transfection. (M) The GTP-agarose pull-down assay of Rab11a in HK-2 cells with or without NAT10 overexpression. (N) The GTP-agarose pull-down assay of Rab11a in K145R-mutant HK-2 cells with or without NAT10 overexpression. Data are presented as mean ± SD. One-way ANOVA was used for comparison between multiple groups; $*P < 0.05$; $**P < 0.01$; $***P < 0.001$.

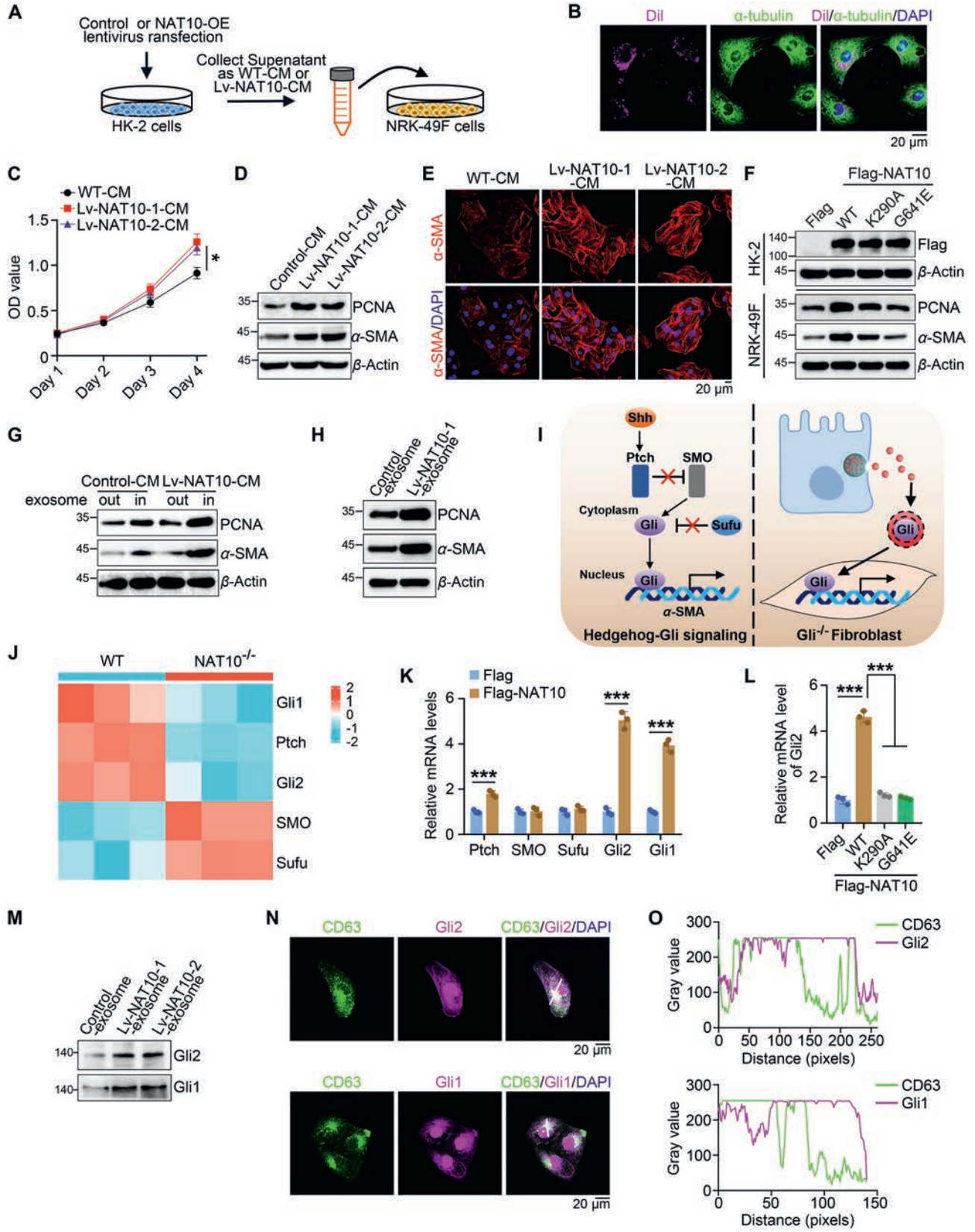

Figure 8 NAT10 upregulates the abundance of Gli2 and Gli1 in TEC-derived exosomes. (A) The diagram demonstrating the experimental design to validate the TEC-fibroblast communication. The conditioned media (CM) collected from wild-type and NAT10-stably-expressed HK-2 cells were used to treat NRK-49F cells. (B) The immunofluorescence staining of Dil and α-tubulin in NRK-49F cells with indicated treatment. (C) The CCK8 analysis of NRK-49F cells ($n = 3$) treated with CM from indicated HK-2 cells. (D) The immunoblot analysis of PCNA and

3.10. Remodelin is a promising therapy for renal fibrosis without downregulating FOXP3 or inducing carcinogenesis

We next tested whether Remodelin was effective in renal fibrosis. First, we found that Remodelin suppressed the expression of Cortactin, USP32 and Gli2 (Fig. 10A and B), and inhibited the acetylation of Rab11a (Fig. 10C). Next, we investigated the effect of Remodelin *in vivo*. Remodelin (10 mg/kg) was injected intraperitoneally in mice with UUO treatment (Fig. 10D). We found that the kidneys from Remodelin-treated mice showed attenuated ECM accumulation and fibroblast activation (Fig. 10E−G). We further validated that Remodelin was effective in uIRI and FA models (Fig. 10H and I).

TGF-β is the most well-known driver of organ fibrosis, however, the therapies targeting TGF-β signaling showed disappointing clinical outcomes, largely because TGF-β signaling is indispensable in maintaining FOXP3 expression in regulatory T cell (Treg), which plays anti-inflammatory and anti-fibrotic roles in kidney[29,41]. We thus wondered whether targeting NAT10, the downstream of TGF-β, affected FOXP3 upregulation upon TGF-β and anti-CD3. We first found that TGF-β inhibitor SB431542 or Smad3 inhibitor SIS3 both reversed TGF-β-induced FOXP3 upregulation in EL4 cells, the cancer cell maintaining T cell properties. In contrast, Remodelin almost showed no influence (Fig. 10J). Similar results were found in $CD4^+CD25^-$ T cells (Fig. 10K). Meanwhile, Remodelin treatment alone did not affect FOXP3 expression in $CD4^+CD25^+$ Treg cells (Fig. 10L). These findings suggested that Targeting NAT10 with Remodelin did not affect TGF-β−Smad3−FOXP3 axis. Additionally, TGF-β is a double-edged sword in cancer, and TGF-β targeting might induce renal carcinogenesis[42]. To this end, we examined whether Remodelin affected proliferation of renal cancer cell lines including Caki-1 and A498 cells. Surprisingly, Remodelin induced a decreased proliferation of both cells rather than an increased one (Fig. 10M and N). Further, we found that Remodelin treatment largely alleviated carcinogenesis of Caki-1 cells *in vivo* (Fig. 10O and P). Taken together, targeting NAT10 with Remodelin might be a viable strategy for renal fibrosis without the side effects of TGF-β targeting.

4. Discussion

In this study, the fundamental role of acetyltransferase NAT10 in TEC-exosome-fibroblast chain and renal fibrogenesis was first uncovered. High-throughout compound screen and clinical analysis revealed targeting NAT10 with Remodelin effectively broke the TEC-fibroblast chain. In response to TGF-β, NAT10 was upregulated mainly in TEC during renal fibrogenesis, and NAT10 specific deletion in TEC greatly mitigated fibroblast activation and renal fibrosis. Next, mechanistic study indicated that nuclear NAT10 and cytoplasmic NAT10 coordinated ac4C and Kac to promote exosome secretion and thus fibroblast activation. More than that, NAT10 also elevated the abundance of exosomal Gli1/2, and exosomal Gli1/2 from TEC act as indispensable driver of fibroblast activation even in the absence of endogenous Gli1/2 in fibroblast. Finally, we found that Remodelin inhibited fibroblast activation and renal fibrosis without affecting FOXP3 expression and renal carcinogenesis. In summary, we proposed targeting NAT10 as a promising strategy for renal fibrosis.

We proposed NAT10 as promising target for renal fibrosis with *in vitro* and *in vivo* experiments, we found that the relative mitigating rate of NAT10 depletion is 55.05%, and the Cohen's d is 2.473, and the relative mitigating rate of Remodelin is 74.7%, and the Cohen's d is 1.844. These data initially implied the translational potential of NAT10 targeting for renal fibrosis. However, the clinical applicability of NAT10 in renal fibrosis is still far and uncertain. For example, the TGF-β-targeted strategy has been frequently proved to be effectively anti-fibrotic in many organs, but it has shown no encouraging outcomes clinically. In addition, the therapeutic potential of NAT10 still needs further validation. This study utilized an *in vitro* model of TEC-fibroblast communication with cell lines including HK-2 and NRK-49F cells. In reality, the TEC-fibroblast communication in human kidney involves other influence factors such as spatial complexity and retrograde fibroblast-TEC communication, which are not fully reflected by the simplified *in vitro* model. Besides, in terms of *in vivo* experiments, UUO, IRI and FA models were used to mimic renal fibrogenesis. Although the above models are the most frequently-used models, there remain other *in vivo* models, especially the disease-associated models such as diabetic kidney disease (DKD) model. Therefore, in the future, whether NAT10 targeting with Remodelin blocks TEC-fibroblast chain and renal fibrosis should be confirmed in other *in vivo* models of renal fibrogenesis. Next, considering that NAT10 exerts pro-fibrotic effect *via* functioning in TEC, how to deliver NAT10 into TEC should be developed. Besides the single usage, whether combined usage of Remodelin with the other drugs will benefit CKD patients, needs further investigation. For example, Remodelin, which inhibits fibroblast activation, might cooperate with other antioxidant or anti-inflammatory drugs to suppress renal fibrosis. Combined usage of Remodelin with inhibitors of other canonical pro-fibrotic signaling might be another option.

Currently, NAT10 is the only acetyltransferase capable of catalyzing both RNA ac4C and protein Kac. However, the studies involving NAT10 all focused on ac4C or Kac. Logistically

α-SMA in NRK-49F cells treated with CM from indicated HK-2 cells. (E) The immunofluorescence staining of α-SMA in NRK-49F cells treated with CM from indicated HK-2 cells. (F) The immunoblot analysis of PCNA and α-SMA in NRK-49F cells treated with CM from HK-2 cells with indicated treatments. (G) The immunoblot analysis of PCNA and α-SMA in NRK-49F cells treated with CM from indicated HK-2 cells with or without exosome removal. (H) The immunoblot analysis of PCNA and α-SMA in NRK-49F cells treated with the same amounts of exosomes from HK-2 cells with or without NAT10 overexpression. (I) The diagram demonstrating the role of TEC-derived exosomal Gli in activation of $Gli^{-/-}$ fibroblast. (J) The heatmap demonstrating the expression profiles of indicated components of Hedgehog-Gli signaling in wild-type ($n = 3$) and NAT10-depleted HK-2 cells ($n = 3$). (K) The qRT-PCR analysis of Ptch, SMO, Sufu, Gli2 and Gli1 in HK-2 cells with or without Flag-NAT10 transfection ($n = 3$). (L) The qRT-PCR analysis of Gli2 in HK-2 cells transfected with wild-type or mutant NAT10 plasmid respectively ($n = 3$). (M) The immunoblot analysis of Gli1 and Gli2 in exosomes derived from indicated HK-2 cells. (N, O) The immunofluorescence staining and quantitative analysis of colocalization of CD63 and Gli1 or Gli2 in HK-2 cells. Data are presented as mean ± SD. Student's *t* test was used for comparison between two groups and one-way ANOVA was used for comparison between multiple groups; $*P < 0.05$; $**P < 0.01$; $***P < 0.001$.

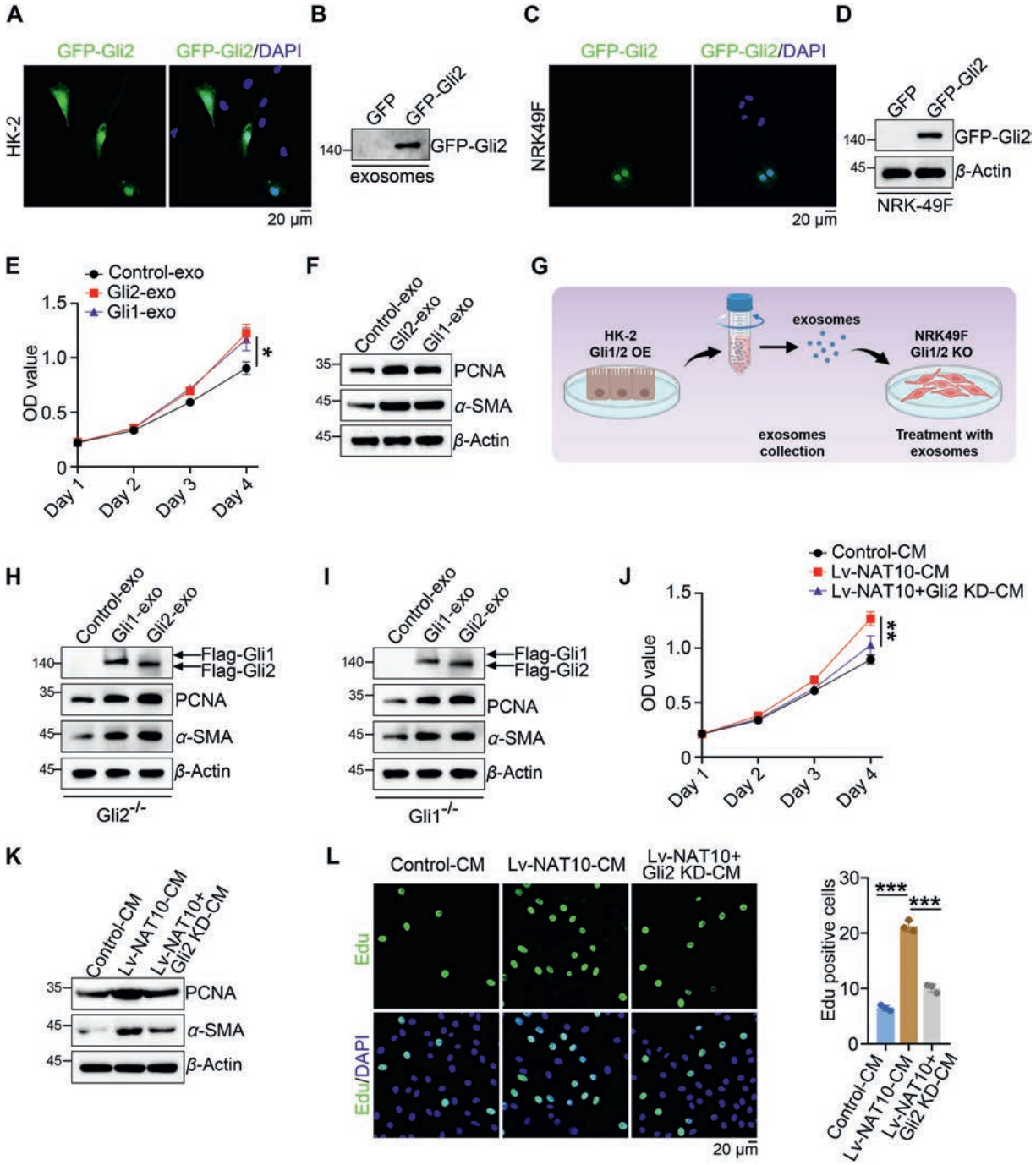

Figure 9 Exosomal Gli1/2 from TEC plays an indispensable role in fibroblast activation. (A) The immunofluorescence staining of GFP in HK-2 cells transfected with GFP-Gli2. (B) The immunoblot analysis of GFP-GFP2 in exosomes derived from HK-2 cells transfected with GFP-Gli2. (C) The immunofluorescence staining of GFP in NRK-49F cells treated with exosomes collected from HK-2 cells transfected with GFP-Gli2. (D) The immunoblot analysis of GFP in NRK-49F cells treated with exosomes collected from HK-2 cells transfected with GFP-Gli2. (E) The CCK8 analysis of NRK-49F cells ($n = 3$) treated with exosomes collected from HK-2 cells transfected with Flag-Gli1 or Flag-Gli2. (F) The immunoblot analysis of PCNA and α-SMA in NRK-49F cells treated with exosomes collected from HK-2 cells transfected with Flag-Gli1 or Flag-Gli2. (G) The graph demonstrating the experimental design to examine the function of exosomal Gli1/2 in fibroblast activation in the absence of endogenous Gli1/2. (H) The immunoblot analysis of PCNA and α-SMA in Gli2-depleted NRK-49F cells treated with exosomes collected from HK-2 cells transfected with Flag-Gli1 or Flag-Gli2. (I) The immunoblot analysis of PCNA and α-SMA in Gli1-depleted NRK-49F cells treated with exosomes collected from HK-2 cells transfected with Flag-Gli1 or Flag-Gli2. (J) The CCK8 analysis of NRK-49F cells ($n = 3$) treated with wild-type and NAT10-overexpressed HK-2 cells with or without Gli2 silencing. (K) The immunoblot analysis of PCNA and α-SMA in NRK-49F cells treated with wild-type and NAT10-overexpressed HK-2 cells with or without Gli2 silencing. (L) The Edu staining and quantitative analysis of NRK-49F cells ($n = 3$) treated with wild-type and NAT10-overexpressed HK-2 cells with or without Gli2 silencing. Data are presented as mean ± SD. Student's *t* test was used for comparison between two groups and one-way ANOVA was used for comparison between multiple groups; $^*P < 0.05$; $^{**}P < 0.01$; $^{***}P < 0.001$.

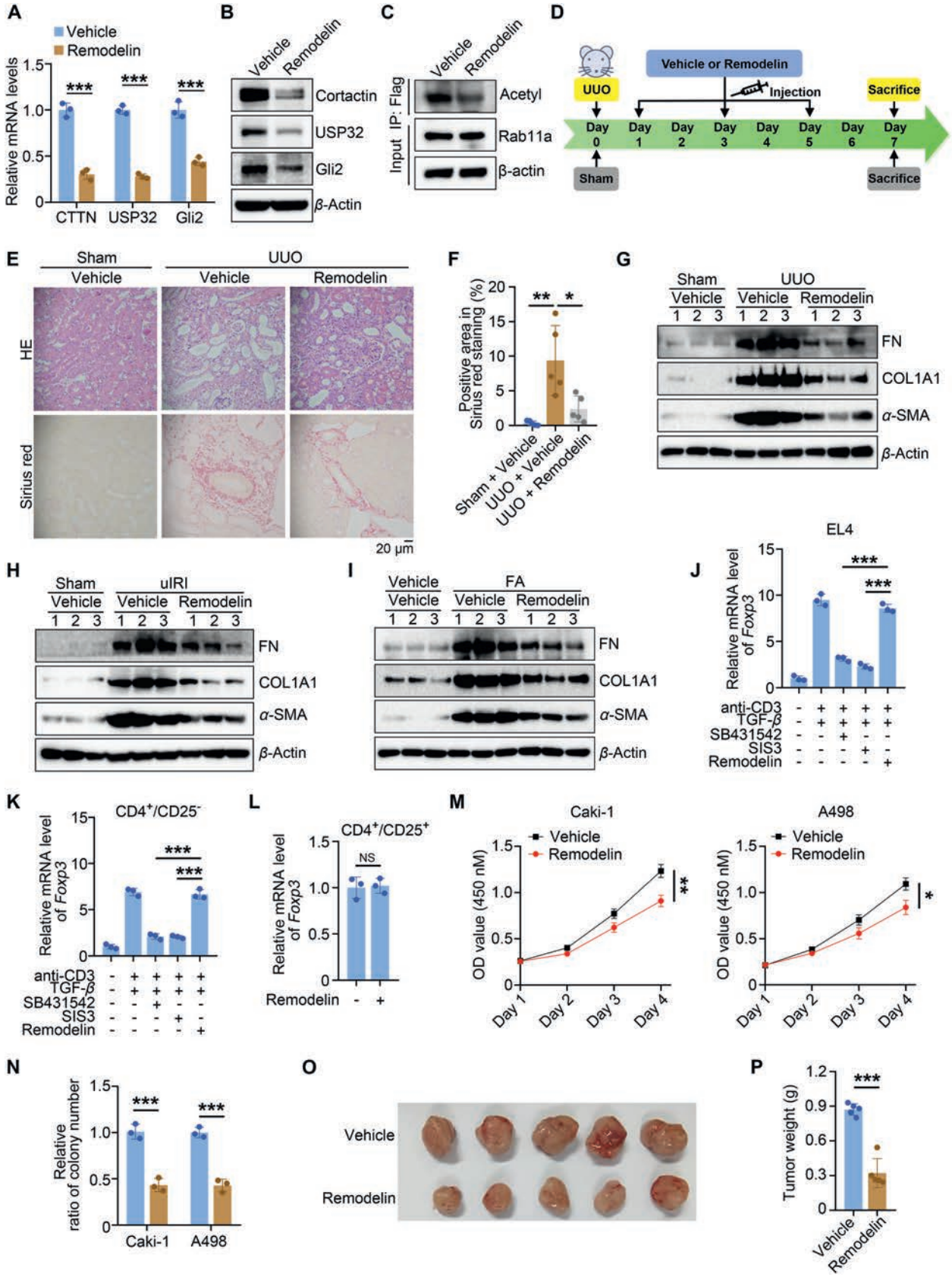

Figure 10 Remodelin is a promising therapy for renal fibrosis without downregulating FOXP3 or inducing carcinogenesis. (A) The qRT-PCR analysis of Cortactin, USP32 and Gli2 in HK-2 cells with or without Remodelin treatment ($n = 3$). (B) The immunoblot analysis of Cortactin, USP32 and Gli2 in HK-2 cells with or without Remodelin treatment. (C) The Co-IP and immunoblot analysis of acetylated-RAB11a in HK-2 cells

speaking, NAT10 should function *via* both ac4C and Kac. This study first reported a NAT10-mediated synergistic effect between ac4C and Kac, in promoting exosome secretion. The exosome secretion is mainly composed of MVB−plasma fusion, invadopodia formation and actin reorganization[36]. Although MVB−plasma fusion is the decisive step among them, they are highly organized and inter-related. Invadopodia formation and actin reorganization are required for wide and stable MVB−plasma fusion, and MVB−plasma fusion favors invadopodia formation in turn. Rab35, Cortactin and Rab11a all function in MVB−plasma fusion[36,43]. Specifically, Rab11a directly drives MVB−plasma fusion *via* SNARE, the executor of MVB−plasma membrane fusion, and Rab35 and Cortactin function in actin reorganization and invadopodia formation[36,44]. Therefore, the cytoplasmic NAT10−Kac axis directly drives MVB−plasma fusion *via* Rab11a, initiating MVB−plasma fusion. Meanwhile, the nuclear NAT10−ac4C axis upregulates Rab35 and Cortactin to advance the MVB−plasma fusion and achieve the exosome secretion on invadopodia. In short, the synergistic effect of nuclear NAT10−ac4C axis and cytoplasmic NAT10−Kac axis in TEC is to simultaneously activate all three major processes of exosome secretion, strongly favoring exosome secretion of TEC (Fig. S8C). It's also interesting to note that this study also highlighted the potential of non-nuclear fractions of NAT10, which was largely ignored. We and others previously reported the roles of membranous NAT10 in carcinogenesis and premature-aging disease[17,45]. This study first reported the function of cytoplasmic NAT10. NAT10 is also expressed in mitochondrial and extracellular space, suggesting that non-nuclear NAT10 deserves more attentions.

Our manuscript proposed targeting NAT10 with Remodelin as potential therapy for renal fibrosis. However, the possible nephrotocity of Remodelin was the first concern. High dose (30 μmol/L) of Remodelin did not affect the cell viability of both HK-2 and NRK-52E cells (Supporting Information Fig. S8A). Next, the *in vivo* toxicity test was performed[46]. Mice were administered with Remodelin daily by oral gavage at 100 mg/kg/day for 4 weeks. After Remodelin administration, no mice died, and no negative effect on renal function was found (Fig. S8B). Although the renal safety of Remodelin was preliminarily validated, more preclinical experiments and further clinical trials are still required. In addition, in another study investigating NAT10's role in renal aging, no significant difference in lifespan and renal function between wild-type mice and *Nat10*-cKO mice was found. More than that, we found that NAT10 abundance increased in aged kidneys (Fig. S2C), and that conditional NAT10 knockout relieved aging-induced fibrogenesis (Fig. S2D). These evidences suggested NAT10 as a safe therapeutic target for renal diseases.

NAT10-targeting strategy is still facing various challenges. Off-target effect is the main one. Although no other targets of Remodelin have been found, to minimize the risk of off-target is still required. Besides increasing the targeting specificity of therapies, developing the kidney-specific delivery of NAT10-targeted therapy will limit the effects in kidney, at least avoiding systematic off-target effects in other organs. More than that, to accurately inhibit the binding of NAT10 with its downstream mRNA or protein with antisense oligonucleotide (ASO) or peptide may be a more specific solution to block NAT10's pro-fibrotic effect. On the other hand, the individual heterogeneity of CKD patients should be considered. NAT10 targeting is not suitable for all CKD patients. In light of this, biomarker-based classification helps to improve the responsiveness of patients to NAT10 targeting. The expression or activation status of NAT10 and its downstream targets in patients should be tested to assess whether NAT10 targeting is potentially beneficial.

5. Conclusions

In summary, our study identified the tubular NAT10 as a molecular switch of TEC-fibroblast communication and renal fibrogenesis *in vivo* and *in vitro*. NAT10 functions *via* promoting the secretion of TEC-derived exosomes and upregulating the abundance of pro-fibrotic cargo in these exosomes. Mechanistically, the nuclear NAT10-ac4C axis and the cytoplasmic NAT10-Kac axis cooperate to facilitate the TEC-fibroblast communication. Targeting NAT10 with Remodelin is a promising strategy for renal fibrosis.

Study approval

All animal experiments were approved by the Laboratory Animal Ethics Committee of Southern China Agricultural University. This study was approved by the Ethics Committee of The Third Affiliated Hospital of Sun Yat-sen University.

Acknowledgements

This research was supported by the Science and Technology Planning Project of Guangzhou(Nos.2024B03J0172); the National Natural Science Foundation of China (Nos. 82370756, 82470784, 82470785 and 82203381); the Science and Technology Planning Project of Guangzhou (Nos. 2025A03J3198).

Author contributions

Tong Zheng and Ning Na designed the project and supervised the manuscript. Tong Zheng, Ning Na, Yuqin Tan and Jiaojiao Zheng

with or without Remodelin treatment. (D) The graph demonstrating the *in vivo* experiment to examine the effect of Remodelin in UUO model. (E, F) The HE staining and Sirius Red staining and quantitative analysis in kidneys from sham mice ($n = 5$) and UUO mice ($n = 5$) with or without Remodelin injection. (G) The immunoblot analysis of fibronectin, collagen I and α-SMA in kidneys from sham mice ($n = 3$) and UUO mice ($n = 3$) with or without Remodelin injection. (H) The immunoblot analysis of fibronectin, collagen I and α-SMA in kidneys from sham mice ($n = 3$) and IRI mice ($n = 3$) with or without Remodelin injection. (I) The immunoblot analysis of fibronectin, collagen I and α-SMA in kidneys from control mice ($n = 3$) and FA mice ($n = 3$) with or without Remodelin injection. (J) The qRT-PCR analysis of *Foxp3* in EL4 cells with the indicated treatment ($n = 3$). (K) The qRT-PCR analysis of *Foxp3* in $CD4^+CD25^-$ T cells with indicated treatment ($n = 3$). (L) The qRT-PCR analysis of *Foxp3* in $CD4^+CD25^+$ Treg cells with indicated treatment ($n = 3$). (M) The CCK8 analysis in Caki-1 cells (left) and A498 cells (right) with or without Remodelin treatment ($n = 3$). (N) The colony formation analysis in Caki-1 cells and A498 cells with or without Remodelin treatment ($n = 3$). (O, P) The tumor formation experiment of Caki-1 cells with or without Remodelin injection ($n = 5$). Data are presented as mean ± SD. One-way ANOVA was used for comparison between multiple groups; $^*P < 0.05$; $^{**}P < 0.01$; $^{***}P < 0.001$.

provided fundings. Yuqin Tan and Jiaojiao Zheng designed and performed the experiments and wrote the manuscript. Ruojiao Wang and Zhaozhong Zhong performed the experiments. Suxiang Chen, Shuo Lu, Jiayu Zheng and Yongrong Ye provided instructions and helped in experiments. All authors approved the final version of the manuscript.

Conflicts of interest

The authors declare no competing interests.

Appendix A. Supporting information

Supporting information to this article can be found online at https://doi.org/10.1016/j.apsb.2026.05.020.

References

1. Qi R, Yang C. Renal tubular epithelial cells: the neglected mediator of tubulointerstitial fibrosis after injury. *Cell Death Dis* 2018;**9**:1126.
2. Aparicio-Trejo OE, Aranda-Rivera AK, Osorio-Alonso H, Martinez-Klimova E, Sanchez-Lozada LG, Pedraza-Chaverri J, et al. Extracellular vesicles in redox signaling and metabolic regulation in chronic kidney disease. *Antioxidants (Basel)* 2022;**11**:356.
3. Van de Vlekkert D, Demmers J, Nguyen XX, Campos Y, Machado E, Annunziata I, et al. Excessive exosome release is the pathogenic pathway linking a lysosomal deficiency to generalized fibrosis. *Sci Adv* 2019;**5**:eaav3270.
4. Liu X, Miao J, Wang C, Zhou S, Chen S, Ren Q, et al. Tubule-derived exosomes play a central role in fibroblast activation and kidney fibrosis. *Kidney Int* 2020;**97**:1181−95.
5. Zhao S, Li W, Yu W, Rao T, Li H, Ruan Y, et al. Exosomal miR-21 from tubular cells contributes to renal fibrosis by activating fibroblasts *via* targeting PTEN in obstructed kidneys. *Theranostics* 2021; **11**:8660−73.
6. Zhou X, Zhao S, Li W, Ruan Y, Yuan R, Ning J, et al. Tubular cell-derived exosomal miR-150-5p contributes to renal fibrosis following unilateral ischemia-reperfusion injury by activating fibroblast *in vitro* and *in vivo*. *Int J Biol Sci* 2021;**17**:4021−33.
7. Li X, Fan X, Yin X, Liu H, Yang Y. Alteration of N(6)-methyladenosine epitranscriptome profile in unilateral ureteral obstructive nephropathy. *Epigenomics* 2020;**12**:1157−73.
8. Tan Y, Zheng T, Su Z, Chen M, Chen S, Zhang R, et al. Alternative polyadenylation reprogramming of MORC2 induced by NUDT21 loss promotes KIRC carcinogenesis. *JCI Insight* 2023;**8**:e162893.
9. Tan Y, Zheng T, Zhang R, Chen S, Cheng Q, Zhang J, et al. Alternative polyadenylation writer CSTF2 forms a positive loop with FGF2 to promote tubular epithelial-mesenchymal transition and renal fibrosis. *Biochim Biophys Acta Mol Basis Dis* 2022;**1868**:166541.
10. Zheng T, Tan Y, Qiu J, Xie Z, Hu X, Zhang J, et al. Alternative polyadenylation trans-factor FIP1 exacerbates UUO/IRI-induced kidney injury and contributes to AKI−CKD transition *via* ROS−NLRP3 axis. *Cell Death Dis* 2021;**12**:512.
11. Liu E, Lv L, Zhan Y, Ma Y, Feng J, He Y, et al. METTL3/N6-methyladenosine/miR-21-5p promotes obstructive renal fibrosis by regulating inflammation through SPRY1/ERK/NF-kappaB pathway activation. *J Cell Mol Med* 2021;**25**:7660−74.
12. Xing J, He YC, Wang KY, Wan PZ, Zhai XY. Involvement of YTHDF1 in renal fibrosis progression *via* up-regulating YAP. *FASEB J* 2022;**36**:e22144.
13. Arango D, Sturgill D, Alhusaini N, Dillman AA, Sweet TJ, Hanson G, et al. Acetylation of cytidine in mRNA promotes translation efficiency. *Cell* 2018;**175**:1872-86.e24.
14. Tsai K, Jaguva Vasudevan AA, Martinez Campos C, Emery A, Swanstrom R, Cullen BR. Acetylation of cytidine residues boosts HIV-1 gene expression by increasing viral RNA stability. *Cell Host Microbe* 2020;**28**:306-12.e6.
15. Dalhat MH, Mohammed MRS, Alkhatabi HA, Rehan M, Ahmad A, Choudhry H, et al. NAT10: an RNA cytidine transferase regulates fatty acid metabolism in cancer cells. *Clin Transl Med* 2022;**12**:e1045.
16. Zheng J, Tan Y, Liu X, Zhang C, Su K, Jiang Y, et al. NAT10 regulates mitotic cell fate by acetylating Eg5 to control bipolar spindle assembly and chromosome segregation. *Cell Death Differ* 2022;**29**: 846−60.
17. Tan Y, Zheng J, Liu X, Lu M, Zhang C, Xing B, et al. Loss of nucleolar localization of NAT10 promotes cell migration and invasion in hepatocellular carcinoma. *Biochem Biophys Res Commun* 2018; **499**:1032−8.
18. Tone Y, Furuuchi K, Kojima Y, Tykocinski ML, Greene MI, Tone M. Smad3 and NFAT cooperate to induce Foxp3 expression through its enhancer. *Nat Immunol* 2008;**9**:194−202.
19. Qi W, Johnson DW, Vesey DA, Pollock CA, Chen X. Isolation, propagation and characterization of primary tubule cell culture from human kidney. *Nephrology* 2007;**12**:155−9.
20. Springall T, Sheerin NS, Abe K, Holers VM, Wan H, Sacks SH. Epithelial secretion of C3 promotes colonization of the upper urinary tract by *Escherichia coli*. *Nat Med* 2001;**7**:801−6.
21. Feng Z, Li K, Qin K, Liang J, Shi M, Ma Y, et al. The LINC00623/NAT10 signaling axis promotes pancreatic cancer progression by remodeling ac4C modification of mRNA. *J Hematol Oncol* 2022;**15**:112.
22. Wang P, Luo ML, Song E, Zhou Z, Ma T, Wang J, et al. Long noncoding RNA lnc-TSI inhibits renal fibrogenesis by negatively regulating the TGF-beta/Smad3 pathway. *Sci Transl Med* 2018;**10**: eaat2039.
23. Song L, Tang S, Han X, Jiang Z, Dong L, Liu C, et al. KIBRA controls exosome secretion *via* inhibiting the proteasomal degradation of Rab27a. *Nat Commun* 2019;**10**:1639.
24. Yan Q, Zhou J, Wang Z, Ding X, Ma X, Li W, et al. NAT10-dependent N^4-acetylcytidine modification mediates PAN RNA stability, KSHV reactivation, and IFI16-related inflammasome activation. *Nat Commun* 2023;**14**:6327.
25. Chen YT, Jhao PY, Hung CT, Wu YF, Lin SJ, Chiang WC, et al. Endoplasmic reticulum protein TXNDC5 promotes renal fibrosis by enforcing TGF-beta signaling in kidney fibroblasts. *J Clin Investig* 2021;**131**:e143645.
26. Chen S, Zhang M, Li J, Huang J, Zhou S, Hou X, et al. Beta-catenin-controlled tubular cell-derived exosomes play a key role in fibroblast activation *via* the OPN−CD44 axis. *J Extracell Vesicles* 2022;**11**: e12203.
27. Yu B, Ouyang L. Epigenetic regulation and drug discovery for cancer therapy. *Curr Top Med Chem* 2019;**19**:971.
28. Cheng Q, Zhang J, Zheng T, Na N. Editorial: innate immunity and renal transplantation. *Front Immunol* 2023;**14**:1206683.
29. Meng XM, Nikolic-Paterson DJ, Lan HY. TGF-beta: the master regulator of fibrosis. *Nat Rev Nephrol* 2016;**12**:325−38.
30. Han X, Wang C, Song L, Wang X, Tang S, Hou T, et al. KIBRA regulates amyloid beta metabolism by controlling extracellular vesicles secretion. *EBioMedicine* 2022;**78**:103980.
31. Xu M, Ji J, Jin D, Wu Y, Wu T, Lin R, et al. The biogenesis and secretion of exosomes and multivesicular bodies (MVBs): intercellular shuttles and implications in human diseases. *Genes Dis* 2023;**10**: 1894−907.
32. Hu SQ, Zou YP, Jiang YQ, Zhang QC, Cheng HX, Wang HR, et al. Scutellarin-mediated autophagy activates exosome release of rat nucleus pulposus cells by positively regulating Rab8a *via* the PI3K/PTEN/Akt pathway. *Cell Biol Int* 2022;**46**:1588−603.
33. Wang T, Gilkes DM, Takano N, Xiang L, Luo W, Bishop CJ, et al. Hypoxia-inducible factors and RAB22A mediate formation of microvesicles that stimulate breast cancer invasion and metastasis. *Proc Natl Acad Sci U S A* 2014;**111**:E3234−42.
34. Hsu C, Morohashi Y, Yoshimura S, Manrique-Hoyos N, Jung S, Lauterbach MA, et al. Regulation of exosome secretion by Rab35 and

its GTPase-activating proteins TBC1D10A-C. *J Cell Biol* 2010;**189**: 223−32.
35. Sinha S, Hoshino D, Hong NH, Kirkbride KC, Grega-Larson NE, Seiki M, et al. Cortactin promotes exosome secretion by controlling branched actin dynamics. *J Cell Biol* 2016;**214**:197−213.
36. Han QF, Li WJ, Hu KS, Gao J, Zhai WL, Yang JH, et al. Exosome biogenesis: machinery, regulation, and therapeutic implications in cancer. *Mol Cancer* 2022;**21**:207.
37. Messenger SW, Woo SS, Sun Z, Martin TFJ. A Ca^{2+}-stimulated exosome release pathway in cancer cells is regulated by Munc13-4. *J Cell Biol* 2018;**217**:2877−90.
38. Meng T, Chen X, He Z, Huang H, Lin S, Liu K, et al. ATP9A deficiency causes ADHD and aberrant endosomal recycling *via* modulating RAB5 and RAB11 activity. *Mol Psychiatr* 2023;**28**:1219−31.
39. Li L, Fu H, Liu Y. The fibrogenic niche in kidney fibrosis: components and mechanisms. *Nat Rev Nephrol* 2022;**18**:545−57.
40. Yang L, Xie G, Fan Q, Xie J. Activation of the hedgehog-signaling pathway in human cancer and the clinical implications. *Oncogene* 2010;**29**:469−81.
41. Gu YY, Liu XS, Huang XR, Yu XQ, Lan HY. TGF-beta in renal fibrosis: triumphs and challenges. *Future Med Chem* 2020;**12**: 853−66.
42. Carreira V, Standeven AM, Ma JY, Hardisty J, Cohen SM, Kerns WD, et al. Inhibitors of TGFbetaR1/ALK4/JNK3/Flt1 kinases in *Cynomolgus macaques* lead to the rapid induction of renal epithelial tumors. *Toxicol Sci* 2021;**180**:51−61.
43. Bai S, Hou W, Yao Y, Meng J, Wei Y, Hu F, et al. Exocyst controls exosome biogenesis *via* Rab11a. *Mol Ther Nucleic Acids* 2022;**27**: 535−46.
44. Yoon TY, Munson M. SNARE complex assembly and disassembly. *Curr Biol* 2018;**28**:R397−401.
45. Larrieu D, Britton S, Demir M, Rodriguez R, Jackson SP. Chemical inhibition of NAT10 corrects defects of laminopathic cells. *Science* 2014;**344**:527−32.
46. Balmus G, Larrieu D, Barros AC, Collins C, Abrudan M, Demir M, et al. Targeting of NAT10 enhances healthspan in a mouse model of human accelerated aging syndrome. *Nat Commun* 2018;**9**:1700.